Characterization of Fault Roughness at Various Scales: Implications of Three-Dimensional High Resolution Topography Measurements

Thibault Candela, François Renard, Michel Bouchon, Alexandre Brouste, David Marsan, Jean Schmittbuhl, Christophe Voisin

Characterization of Fault Roughness at Various Scales: Implications of Three-Dimensional High Resolution Topography Measurements

Thibault Candela [1], François Renard [1, 2], Michel Bouchon [3], David Marsan[4], Jean Schmittbuhl[5], and Christophe Voisin [3]

(1) University Joseph Fourier Grenoble I, Laboratoire de Géodynamique des Chaînes Alpines, CNRS, BP 53, 38041 Grenoble, France (Thibault.Candela@bvra.e.ujf-grenoble.fr, françois.renard@ujf-grenoble.fr).

(2) Physics of Geological Processes, University of Oslo, Oslo, Norway.

(3) University Joseph Fourier Grenoble I, Laboratoire de Géophysique Interne et Tectonophysique, CNRS, Grenoble, France (christophe.voisin@ujf-grenoble.fr, michel.bouchon@ujf-grenoble.fr).

(4) University of Savoie, Laboratoire de Géophysique Interne et Tectonophysique, CNRS, Le Bourget du Lac, France (david.marsan@univ-savoie.fr)

(5) UMR 7516, Institut de Physique du Globe de Strasbourg, Strasbourg, France.

Short title: Roughness of fault surfaces

Abstract – Accurate description of the topography of active faults surfaces represents an important geophysical issue because this topography is strongly related to the stress distribution along fault planes, and therefore to processes implicated in earthquake nucleation, propagation, and arrest.

Up to know, due to technical limitations, studies of natural fault roughness either performed using laboratory or field profilometers, were obtained mainly from 1D profiles. With the recent development of Light Detection And Ranging (LIDAR) apparatus, it is now possible to measure accurately the 3D topography of rough surfaces with a comparable resolution in all directions, both at field and laboratory scales. In the present study, we have investigated the scaling properties including possible anisotropy properties of several outcrops of two natural fault surfaces (Vuache strike-slip fault, France, and Magnola normal fault, Italy) in limestones. At the field scale, digital elevation models of the fault roughness were obtained over surfaces of 0.25 m^2 to 600 m^2 with a height resolution ranging from 0.5 mm to 20 mm. At the laboratory scale, the 3D geometry was measured on two slip planes, using a laser profilometer with a spatial resolution of 20 μm and a height resolution less than 1 μm.

Several signal processing tools exist for analyzing the statistical properties of rough surfaces with self-affine properties. Among them we used six signal processing techniques: (i) the root-mean-square correlation (RMS), (ii) the maximum-minimum height difference (MM), (iii) the correlation function (COR), (iv) the RMS correlation function (RMS-COR), (v) the Fourier power spectrum (FPS), and (vi) the wavelet power spectrum (WPS). To investigate quantitatively the reliability and accuracy of the different statistical methods, synthetic self-affine surfaces were generated with azimuthal variation of the scaling exponent, similar to what is observed for natural fault surfaces. The accuracy of the signal processing techniques is assessed in terms of the difference between the “input” self-affine exponent used for the synthetic construction and the “output” exponent recovered by those different methods. Two

kinds of biases have been identified: artifacts inherent to data acquisition and intrinsic errors of the methods themselves. In the latter case, the statistical results of our parametric study provide a quantitative estimate of the dependence of the accuracy with system size and directional morphological anisotropy.

Finally, we used the most reliable techniques (RMS-COR, FPS, WPS). For both field and laboratory data, the topography perpendicular to the slip direction displays a similar scaling exponent $H_{\perp} = 0.8$. However, our analysis indicates that for the Magnola fault surface the scaling roughness exponent parallel to the mechanical striation is identical at large and small scales $H_{//} = 0.6 - 0.7$ whereas for the Vuache fault surface it is characterized by two different self-affine regimes at small and large scales. We interpret this cross-over length scale as a witness of different mechanical processes responsible for the creation of fault topography at different spatial scales.

Key words: fault, 3D laser scanner, fault-surface roughness, self-affine surface, roughness exponent.

1. Introduction

Knowledge of the detailed fault geometry is essential to understand some major processes involved in faulting such as grain comminution or asperities abrasion during slip, geometrical heterogeneity of the stress field that controls earthquake nucleation (CAMPILLO *et al.*, 2001; VOISIN *et al.*, 2002a), rupture propagation, and arrest (VOISIN *et al.*, 2002b). Establishing correlations between geometrical properties of fault roughness (POWER *et al.*, 1987, 1988; POWER and TULLIS, 1991; SCHMITTBUHL *et al*., 1993; LEE and BRUHN, 1996; POWER and DURHAM, 1997; RENARD *et al.*, 2006; SAGY *et al.*, 2007), seismic behavior of faults (OKUBO and AKI, 1987; PARSON, 2008), frictional strength and critical slip distance (SCHOLZ, 2002), wear processes during fault zone evolution (POWER *et al.*, 1988) represents a fundamental issue to understand seismic faulting.

At the laboratory scale, AMITRANO and SCHMITTBUHL (2002) highlight a complex coupling between fault gouge generation and fault roughness development. At larger scale, asperities control the slip distribution of earthquake (PEYRAT *et al.*, 2004). Indeed asperities on active fault planes concentrate the stress (MARSAN, 2006; SCHMITTBUHL *et al.*, 2006) and therefore may control earthquake nucleation (LAY *et al.*, 1982; SCHOLZ, 2002) and the propagation of the rupture to its ultimate arrest (AKI, 1984). High resolution relocations of earthquakes using the multiplet technique have shown streaks of earthquake along several faults in California (RUBIN *et al.*, 1999). This pattern has been interpreted as resulting from the presence of an organized large scale roughness (asperities) resisting slip (SCHAFF *et al.*, 2002).

Despite recent progress in seismology, the imaging of fault planes over a large range of scales at depth is not yet available. A quasi-unique access to high resolution description of the fault plane comes from exhumed fault scarp observations. This requires, of course, that the main morphological patterns of faults mapped at the surface of the earth persist at least across the

seismogenic zone. Due to technical limitations, prior comparative studies of natural fault roughness were mainly based on 1D profilometry (POWER *et al.*, 1987, 1988; POWER and TULLIS, 1991; SCHMITTBUHL *et al.*, 1993; LEE and BRUHN, 1996; POWER and DURHAM, 1997). These 1D measurements have shown that fault roughness can be characterized by a scale invariance property described by a self-affine geometry (see section 2 for the definition of self-affinity) with a roughness scaling exponent close to 0.8 for profiles oriented in a direction perpendicular to the striations observed on the fault plane. Such striations are aligned in the direction of slip. The value of 0.8 is similar to what was measured for tensile cracks (POWER *et al.*, 1987; SCHMITTBUHL *et al.*, 1995b; BOUCHAUD, 1997). Moreover, the influence of slip was also quantified: the fault surfaces have smaller roughness amplitude along the slip direction than perpendicular to it (POWER *et al.*, 1988; POWER and TULLIS, 1991; LEE and BRUHN, 1996; POWER and DURHAM, 1997). The compiled fault roughness statistics of several studies (POWER and TULLIS, 1991; LEE and BRUHN, 1996; BEN-ZION and SAMMIS, 2003) suggest a change in scaling properties between large and short length scales. However, considering the noise in their data, these authors underlined that it was not possible to decipher whether this variation was related to small-scale surface weathering of the fault scarp or to the faulting process itself.

With the recent development of high resolution distancemeters, it is now possible to use accurate statistical approaches to quantify fault roughness. Indeed, portable 3D laser scanners (also called LiDAR, Light Detection And Ranging) allow mapping fault surface outcrops over scales of 0.5 mm to several tens of meters. The accuracy of the measurements enables a reliable quantification of the data. RENARD *et al.* (2006) and SAGY *et al.* (2007) demonstrated precisely the scaling invariance and anisotropy properties of fault topography using ground based LIDAR and laboratory profilometers. In these previous studies, statistical analysis of fault roughness was carried out with a single signal processing tool. However,

SCHMITTBUHL *et al.* (1995a, 1995b) recommend the simultaneous use of different methods in order to appreciate the confidence in the measured scaling invariance properties.

In the present study, we use new roughness data to extend the type of measurements made by RENARD *et al*. (2006) and SAGY *et al.* (2007) and propose a parametric study of the statistical results of fault topography, using multiple signal processing tools. In order to investigate the reliability and accuracy of the different signal processing methods, synthetic self-affine surfaces were generated with azimuthal variation of the scaling exponent. These synthetic rough surfaces are completely characterized by two different self-affine exponents prescribed in perpendicular directions. When comparing these synthetic surfaces to natural faults, one should keep in mind that any self-affine model can only describe a real surface to a finite degree of accuracy, and only within a finite range of scales. After this systematic study, we used the most reliable and accurate techniques to investigate the scaling properties and anisotropy of several outcrops of two natural fault surfaces that have been measured using 3D laser scanners in the field and a laser profilometer in the laboratory.

This paper is organized as follows. In Section 2, following a brief explanatory discussion of the self-affine notion, the generation process of synthetic self-affine surfaces with a directional morphological anisotropy is described. In Section 3, statistical methods to define the self-affine properties are reviewed. Section 4 is devoted to the systematic study of the accuracy of the methods. Section 5 is devoted to the acquisition of data on natural fault. In Section 6, analysis of the roughness, covering six orders of magnitude of length scales, is performed on several outcrops of two natural faults. Finally, in Section 7, we conclude by linking our findings on the statistical properties of natural fault topography to the results of earlier studies, with the ultimate goal of developing a more mutually consistent description of fault asperities geometry.

2. Generation of self-affine surfaces

2.1 Self-affinity in 1D and 2D

Surface roughness analysis provides a statistical characterization of a surface which is simpler and easier to use than a complete deterministic description. In geophysics, BROWN and SCHOLZ (1985) and POWER *et al*. (1987) demonstrated the self-similar property of natural fault surfaces at field scale. Coming from statistical physics, a more general scaling transformation has been proposed: self-affinity (MANDELBROT, 1985; MANDELBROT, 1986; VOSS, 1985) that was successfully used for the quantitative description of fault roughness (SCHMITTBUHL *et al.*, 1993, RENARD *et al.*, 2006).

A self-affine 1D profile remains unchanged under the scaling transformation $\delta x \rightarrow \lambda\, \delta x$, $\delta z \rightarrow \lambda^{H} \delta z$ for 1D profiles (Figure 1) extracted from a surface (MEAKIN, 1998). Here, δx is the coordinate along the profile and δz is the roughness amplitude. For a self-affine profile, the scaling exponent H, also called Hurst exponent, lies in the range $0 \leq H \leq 1$. Accordingly, self-affinity implies that a profile appears less rough as the scale increases. In other words, if a profile is self-affine, a magnified portion of it will appear statistically identical to the entire profile if different magnifications are used in the x and z-directions (Figure 1).

For 2D surfaces, this self-affinity property can be described for sets of 1D parallel profiles extracted from the surface. Moreover, if the surface is striated along some given orientation, anisotropic scaling behavior can emerge if H varies for different directions in the plane of the surface. An anisotropic self-affine surface $Z(x, y)$ with coordinates (x, y) obeys the property: $Z\left(\lambda^{1/H_{//}} x, \lambda^{1/H_{\perp}} y\right) = \lambda\, Z(x, y)$, where λ is a positive dilation factor, $H_{//}$ and $H_{\perp}$ are the Hurst exponents, comprised between 0 and 1, in two perpendicular directions of the surface. $H_{//}$ is defined along a direction parallel to the main striations, and $H_{\perp}$ is defined along a direction perpendicular to the striation (Figure 1b).

2.2 Synthetic anisotropic self-affine surfaces

To calculate synthetic fault surfaces (Figure 1b), we used a Fourier based method to simulate a fractional Brownian motion on a 2D grid (STEIN, 2002), where an anisotropy matrix $E = \begin{pmatrix} 1/H_{//} & 0 \\ 0 & 1/H_{\perp} \end{pmatrix}$ was introduced when calculating the 2D Gaussian random field. The eigenvalues of this matrix correspond to the inverse of the two roughness exponents $H_{//}$, and $H_{\perp}$ that characterize the self-affine properties of the generated surface in two perpendicular directions (BIERME *et al.* 2007, 2008). The code to generate an anisotropic 2D self-affine surface, written in Matlab©, is given in the appendix A and can be run easily on a desktop computer.

In the following sections, we decompose the signal processing analysis of rough surfaces in two stages. Firstly, we present the six signal processing tools used to estimate the self-affine property of an isotropic surface with a single Hurst exponent (Figure 1a), as observed for example for fresh mode I brittle fractures in rocks (POWER *et al.*, 1987; SCHMITTBUHL *et al.*, 1995b; BOUCHAUD, 1997). For this, we have synthesized several isotropic surfaces with an exponent in the range [0.1 - 0.9] and grid sizes in geometrical series: 129 × 129 points, 513 × 513 points, 2049 × 2049 points. Secondly, we analyse synthetic anisotropic surfaces (Figure 1b) with $H_{//}$ in the range [0.7 - 0.9] and $H_{\perp}$ in the range [0.4 - 0.9].

3. Statistical signal processing methods

We have used six different methods that characterize the amplitude of the roughness at various spatial wavelengths. All these methods, presented in the following sub-sections, are based on the analysis of 1D profiles (Figure 1c) that are extracted from the 2D Digital Elevation Model (DEM) of 2D surfaces (Figure 1a, b). For each surface, a set of 1D parallel profiles in a specific direction are extracted, detrended and then analyzed. Then, the properties

194 are averaged over all the 1D profiles to characterize the 2D surface in the chosen direction.
195 We have repeated such analyses for profiles extracted in several directions, following a 360°
196 rotation, allowing then to determine the azimuthal dependence of the statistical properties of
197 the surface (RENARD *et al.*, 2006) that could characterize a morphological anisotropy.
198 For the application to natural fault surfaces, we also tested how the noise in the data and the
199 presence of missing points could affect the estimation of fault surface. Indeed, the raw
200 scanner data consist of clouds of points, with x, y, and z coordinates, sampled more or less
201 regularly. Sometimes, data are missing (vegetation on the fault plane, low reflectivity of the
202 scanner light beam), and the surface is incomplete. An interpolation is then necessary, which
203 induce a bias in the estimation of scaling exponents that need to be estimated too.
204 *3.1 Root-mean-square correlation (RMS) and maximum-minimum height difference (MM)*
205 *methods*
206 Let consider a 1D profile $L(x)$. This profile is divided into windows of width δx and indexed
207 by the position of the first point x_0 of the band. The standard deviation $\sigma(\delta x)$ of the height
208 $L(x)$ and the height difference $h(\delta x)$ between the maximum and minimum height are
209 computed for each band, and then averaged over all the possible bands of fixed width δx
210 spanning the profile, by varying the origin x_0. We then obtain $\langle\sigma(\delta x)\rangle$ and $\langle h(\delta x)\rangle$, where
211 both quantities follow a power law for a self-affine profile: $\langle\sigma(\delta x)\rangle \propto \delta x^H$ and
212 $\langle h(\delta x)\rangle \propto \delta x^H$ (SCHMITTBUHL *et al.* 1995a).
213 Note that these techniques are useful when *H* is not too close from 0 or 1, where a significant
214 error can be measured (see Figures 3a, b – 4a, b). Usually, levelling off of $\sigma(\delta x)$ at small δx
215 values is due to the noise in the data (see Figure 7c, d), and leveling-off at large δx is due to
216 the finite size of the profile.
217

3.2 Height-height correlation function (COR) method

For a signal $L(x)$, we consider the height-height correlation function defined by $C(\Delta x)=\left[\left\langle (L(x)-L(x+\Delta x))^2 \right\rangle\right]^{1/2}$, which estimates the average height-height difference between two points of the profile separated by a distance Δx. For a self-affine profile, the correlation function follows a power-law such that $C(\Delta x)\propto \Delta x^H$ where H is the Hurst exponent.

3.3 Standard deviation of the correlation function (RMS-COR) method

For a profile $L(x)$ containing N points, the height difference ΔL between each couple of points separated by a distance Δx is calculated. The window size Δx is varied between the sampling distance and the size of the system and, for a given Δx, the standard deviation of the height difference $\sigma(\Delta L_{\Delta x})$ is calculated. For a self-affine surface this measurement follows a power-law such that $\sigma(\Delta x)\propto \Delta x^H$. This method was successfully applied to characterize the self-affine properties of the Vuache fault plane (RENARD *et al.* 2006).

3.4 Fourier power spectrum (FPS) method

The Hurst exponent H can be estimated from the Fourier power spectrum which has a power law form for a 1D self-affine profile (BARABASI and STANLEY, 1995; MEAKIN 1998). For each parallel profile, the Fourier power spectrum $P(k)$, *i. e.* the square of the modulus of the Fourier transform, is calculated as a function of the wave-number k. Then the spectrum of the whole surface is calculated by stacking all the 1D Fourier transforms to reduce the noise associated with individual profiles. For each profile of length L containing N increments, the spatial frequencies range between $1/L$ and the Nyquist frequency $N/2L$ (*i.e.* the reciprocal of the interval between data points). When plotting the power spectrum as a function of k in log-log space, a self-affine function reveals a linear slope, which is itself a function of the Hurst exponent H through $P(k)\propto k^{-1-2H}$.

3.5 Average wavelet coefficient power spectrum (WPS) method

The average wavelet coefficient method consists of decomposing the input signal into amplitudes that depend on position and scale. The wavelet transform of each 1D profile $L(x)$ is defined as $W_{a,b} = \frac{1}{\sqrt{a}} \int_{-\infty}^{+\infty} \psi\left(\frac{x-b}{a}\right) L(x) dx$ where ψ is the wavelet function. Then the wavelet coefficients are averaged over the translation factor b for each length scale a: $W_a = \langle W_{a,b} \rangle_b$. If the profile is self-affine, the wavelet transform verifies statistically that, for any positive dilatation factor λ, $W_{a,b}[L(\lambda x)] = \lambda^H W_{a,b}$. Accordingly, the averaged wavelet coefficients scale as $W_a \propto a^{H+1/2}$. A wide range of wavelet functions can be used. For a simple and efficient implementation, we chose the Daubechies wavelet of order 12 as suggested in SIMONSEN *et al*. (1998).

4. Quantitative estimation of the accuracy of roughness analysis methods

4.1 Synthetic isotropic and anisotropic rough surfaces

Figures 1a and 1b display the topography of synthetic rough surfaces where the data set includes 2049 × 2049 points regularly spaced on a grid. Figure 1a shows an isotropic rough surface, whereas Figure 1b shows an anisotropic surface, with corrugations elongated parallel to the direction of smaller Hurst exponent (analogue to the direction of slip on a natural fault surface) and covering a wide range of scales.

The roughness amplitude of a profile parallel to the striation direction (green curve in Figure 1c) is smaller than that of a perpendicular profile. The profile extracted along the direction with the smallest exponent (green curve) appears more jagged at small scales compared to a perpendicular profile, showing the different effects of the anisotropy of the surface on the waviness and amplitude of the profiles.

The outputs of the statistical methods described in section 2.3 are represented on Figure 2 Each curve is calculated by averaging the outputs of all possible parallel 1D profiles extracted from the anisotropic surface of Figure 1b. The results are represented in a log-log plot, allowing visualizing the linear portion of the curve that characterizes a power-law distribution (Figure 2). This linear portion is binned in a small number of increments, and a power-law fit is performed to extract the Hurst exponent that characterizes the self-affinity of the profile. The best fits are performed for each curve and a value of the "output" self-affine exponent is then calculated for all the six signal processing methods.

Using the RMS correlation function, we have also extracted sets of parallel profiles in several directions, at an angle θ to the direction of the striations. For each set of profile, we have calculated the correlation function and estimated the value of H. The angular dependence of H could be represented on a polar plot (inset in Figure 2d) (RENARD *et al.*, 2006). The anisotropy of such plot characterizes the anisotropy of the surface: an isotropic surface is represented as a circle of radius H, whereas an anisotropic one has a more complex elliptical shape.

4.2 Isotropic surfaces: effect of size and input exponent on the output estimation of the Hurst exponent

The comparison between the input Hurst exponent used to calculate an isotropic synthetic surface and the output Hurst exponent estimated using the six different methods is represented on Figure 3, for different system sizes. The RMS, MM, COR and RMS-COR methods are all mainly sensitive to the value of the input self-affine exponent (the typical trend of the curve is not parallel to the diagonal). Small self-affine exponents are systematically overestimated whereas large exponents are underestimated. In contrast, the error for the WPS method is mainly function of the system size (the response is more or less parallel to the diagonal). The FPS method appears the most accurate technique, with only slight sensitivity to the input self-

affine exponent and size effects. This conclusion should however be interpreted cautiously as the algorithm used to generate the synthetic surface is based on a Fourier transform approach. The conclusion of this comparison tests is that the FPS, WPS, and RMS-COR methods are the most reliable because they have a small dependence on the value of the input Hurst exponent and a slight dependence on system size.

4.3 Anisotropic surfaces: Interaction between the two input roughness exponents

For synthetic self-affine anisotropic surfaces, we have calculated the error on the estimation of the two Hurst exponents. For this, we have built surfaces (2049x2049 points, similar to Figure 1b) for which the Hurst exponents $H_{input\,//}$ and $H_{input\perp}$ in two perpendicular directions were varied in the range [0.4 – 0.9]. We have then used the six signal processing techniques to estimate the values of these same exponents. The absolute error in the estimation of each Hurst exponent (Figure 4) depends on the input value of these parameters and also on the amplitude of their difference ($H_{input\,//} - H_{input\perp}$).

This error is particularly large for the RMS (up to 20%), MM (up to 25%), and COR (up to 35%) methods. When the input anisotropy ($H_{input\,//} - H_{input\perp}$) increases, the absolute error on the two output exponents increases accordingly. The absolute error is smaller in the direction of the smallest exponent (analogue to the direction of striation on a natural fault surface) than perpendicular to it. Moreover, it is also noteworthy to mention that these three techniques show significant errors in the estimation for input exponents close to 0.8-0.9 even if the anisotropy is minimal, demonstrating the limited reliability of these methods to detect an exponent close to one.

The RMS-COR analysis is also sensitive to the input anisotropy (Figure 4d), however such an effect is not strongly pronounced (the absolute errors are smaller, up to 15%). For this method, the error does not depend on the values of the two input Hurst exponents. For example, with a synthetic surface defined by $H_{input\,//} = 0.8$ and $H_{input\perp} = 0.6$, the absolute error

315 in the estimation of each Hurst exponent is almost identical. As shown in Figure 4d, when
316 anisotropy is small, the errors do not increase significantly for input values close to 1 unlike
317 the three previous methods.
318 The FPS and WPS analysis are only slightly sensitive to the “input” anisotropy and the
319 estimated Hurst exponents do not depend on the input exponent values. Our analysis clearly
320 shows that the FPS, the WPS and, to a lesser extent, the RMS-COR methods are the most
321 reliable. More precisely, the RMS-COR and the WPS techniques slightly underestimate and
322 overestimate, respectively, the roughness exponent compared to the FPS method.
323 We have also analyzed the azimuthal dependence of the Hurst exponent for synthetic
324 anisotropic self-affine surfaces. Comparisons of the “output” anisotropy estimated using the
325 RMS-COR method and the “input” anisotropy is represented on Figure 5. We have used this
326 technique because it does not require interpolation of the profiles, whereas the FPS and WPS
327 methods would need regularly spaced data point. A significant directional morphological
328 anisotropy of surfaces is visible on these polar plots of H even if a low “input” anisotropy is
329 imposed, thus demonstrating the reliability of the RMS-COR method to detect a slight
330 morphological anisotropy. Remarkably, following a 360° rotation, the azimuth variation of H
331 is not progressive. When departing a few degrees from the direction of the smallest “input”
332 exponent, the “output” exponent is already very close to the largest “input” exponent. This
333 property of anisotropic self-affine surface is not well understood yet.
334 A tentative way to calculate the error on the anisotropy that is made when estimating the
335 anisotropy of the surface $\left|H_{//} - H_{\perp}\right|$ is represented on Figure 6. This plot indicates the error
336 on the estimation of the anisotropy of the surface, and therefore provides some bounds on the
337 accuracy of the determination of this property. Almost all methods underestimate the
338 anisotropy, except the Fourier power spectrum which slightly overestimates it. For the RMS,
339 MM, and COR methods, when the “input” anisotropy $\left|H_{//} - H_{\perp}\right|$ increases, the absolute error

on the “output” anisotropy increases accordingly. Moreover, this absolute error is similar for all surfaces with the same “input” anisotropy, whatever the values of the two “input” self-affine exponents.

The determination of the “output” anisotropy with the RMS-COR, FPS, and WPS methods is less sensitive to the “input” anisotropy, except for the highest anisotropy, thus demonstrating the robustness of these three methods to determine the azimuth dependence of the statistical properties of an anisotropic self-affine surface. More precisely, estimates reported for the WPS method are somehow systematically lower than the two others techniques.

4.4 Effect of noise

In all physical measurements, noise is present in the data because of the limited resolution of the measuring device. Such noise is usually described using Gaussian statistics with a zero mean and a constant variance. We have analyzed how the presence of noise in synthetic data could alter the estimation of the Hurst exponent. For this, we have calculated synthetic anisotropic surfaces and added a Gaussian noise with a standard deviation equal to 1/200 of the standard deviation of the rough surface (Figure 7a, b). This artificial alteration of the synthetic surface mimics measurements biases obtained on natural data, for example due to electronic noise in the measurement device or due to weathering of the fault surface. We have then estimated the Hurst exponents using the six signal processing methods and compared the results with the noise-free analysis. The results confirm that adding noise to the synthetic data induces a leveling-off of the curves at small length scales (RENARD *et al.*, 2006; SAGY *et al.*, 2007) and therefore a possible underestimation of the Hurst exponent, for all the six signal processing methods (Figure 7c-h).

Despite the fact that the Gaussian white noise added is isotropic, each plot (Figure 7c-h) indicates that the effect of noise is slightly dependent on the azimuth of the profile: the underestimation of the Hurst exponent is more pronounced along striations than

perpendicularly to them. Indeed, the addition of noise in the rough signal preferentially alters the roughness at small scales, and therefore has a stronger effect on the profiles parallel to the striations because they are characterized by a smaller amplitude at large length scales compared to the profiles perpendicular to the striations.

For the RMS, MM and RMS-COR methods, the noise does affect not only the small length scales but also the large length scales. Indeed, such an effect is strongly pronounced for these three methods and, slopes of the curves in Figure 7c-f lead to a significant underestimation of the actual value of the self-affine exponents. Notably, the polar plot of H from a surface with added noise obtained with the RMS-COR technique (see Figure 7f) shows errors of 10 % and 20 % on the Hurst exponent measured in directions perpendicular and parallel to striations, respectively.

Conversely, the COR, FPS, and WPS techniques are less sensitive to the addition of noise. At large scale, the noise appears as a negligible correction, and even if the curves are affected at small scales, the estimation of the self-affine exponent is less affected.

4.5 Effect of missing data

When considering natural fault measurements, local weathering and/or the presence of vegetation may form patches of missing data. To study their influence on estimation of fault surface properties, we generated incomplete data sets removing an increasing percentage of clusters of points from a synthetic surface that initially contained 513x513 points (Figure 8).

For the FPS and WPS methods, the incomplete cloud of points was interpolated across the gaps (Figure 8b), using a linear fit. However, for the RMS-COR method, the biased data can be used without interpolation of the holes (Figure 8c).

Typically, in our natural data sets 5 % of interpolated holes is the maximum percentage of spurious points removed from the raw scanner data. The results (Figure 8d-f) indicate that the RMS-COR, FPS and WPS analysis show an error of only 4 % on the Hurst exponent

390 estimated on a surface with 40 % holes compared to a complete surface. Therefore, 5% of
391 missing points does not affect significantly the measurement of surface properties, whatever
392 the technique employed.
393
394 *5. Acquisition of roughness data on natural faults at various scales*
395 *5.1 Acquisition of the data on the field and in the laboratory*
396 The roughness data of several fault samples were acquired at various scales using five
397 different scanning devices (Table 1). At the laboratory scale, we used a home-made laser
398 profilometer (MEHEUST, 2002), where a sample, set on a 2-axis moving table, is scanned by
399 measuring the distance between the sample and a laser head. The horizontal scanning steps
400 are either 20 or 24 micrometers and the vertical resolution is better than 1 micrometer.
401 On field outcrops, we measured several surfaces with four different LIDARs, where two main
402 technologies were used. The S10 system (Table 1) contains a laser source and two cameras;
403 the distance between the laser head and a surface point is measured by triangulation. The
404 maximum shooting distance is around 15 m and the resolution in the distance measurement is
405 close to 0.5 mm. Surfaces of several square meters can be measured with this system. The
406 main drawback of this system is that it must be operated during night time otherwise the day
407 light may blind the cameras.
408 The other three LIDAR systems (Table 1) are based on the same technology and were built by
409 three different companies: a light pulse is sent from a laser head and the time of flight to the
410 target point is measured, allowing calculating the distance, knowing light velocity. The whole
411 target surface is scanned by rotating the laser head at constant angular velocity. The main
412 advantages of this technology is that fast scanning rates can be achieved (up to 5000 points/s),
413 the shooting distance can be as large as 1500 m and the system can be operated even under
414 day light. However, compared to the S10 system, the measurement accuracy is lower,

between 1 and 2 cm. Note also that if the laser wavelength is in the infra-red range, absorption by water present on the target surface might also alter the quality of the data.

We have used these scanning measurement devices on two faults in limestones, where outcrop fault planes were scanned at various scales. Hand samples of slip surfaces were also collected and measured with the laboratory profilometer.

5.2. The Magnola normal fault

The Magnola fault outcrop, in the Fuccino area, is part of the extensive fault system in Central Apenines (Italy). This 15-km long normal fault shows microseismic activity and offsets limestone beds with a vertical displacement larger than 500 meters and a slight shear component witnessed by mechanical striations dipping at a 85° angle on the fault plane. This fault is characterized by recent exhumation (PALUMBO *et al*. 2004, CARCAILLET *et al*. 2008) and the last earthquakes have risen to the surface a ~10-m thick band of fresh limestone (Figure 9a) where mechanical striations and grooves at all scales are still visible and less altered by weathering than older exhumed portions of the fault. We have scanned several sub-surfaces of the fault wall (Table 2, Figure 9b) and collected one hand sample from the roof of the fault for laboratory measurements (Table 2, Figure 9c). This sample, that shows mechanical striations, was dig from below the ground surface, to get a slip surface preserved from climatic weathering. The larger outcrop surfaces show evidence of erosion and some karstic water outlets provided holes for vegetation. Small bushes and grass outcrops had to be removed either directly from the fault plane, of from the LIDAR data. The result was incomplete data sets of the fault surface, with missing points in the records. Nevertheless, elongated bumps and depressions at large scales (Figure 9a), and grooves and ridges at small scales (Figure 9b) aligned parallel to slip can be observed.

5.3. The Vuache strike-slip fault

The Vuache fault is an active strike-slip fault system in the western part of the French Alps (THOUVENOT *et al.* 1998). The fault outcrop we analyzed lies on a short segment that connects to the main Vuache fault and that is not active anymore. This fault was analyzed in RENARD *et al*. (2006) and we present here new data of large and small scale slip surfaces (Figure 10).

This fault has a mainly strike-slip component, witnessed by large elongated bumps and depressions associated with linear striations of smaller size observed at all scales up to the resolution of the scanners LIDAR (Figure 10c, d). Conversely, the laboratory data show that the surface below the centimeter scale appears more polished and only smooth decimeter ridges persist (Figure 10f).

The fault offsets meter-scale beds of limestones and the fault plane was exhumed ten years ago by the activity of a quarry. As a consequence, the LIDAR measurements could be performed on fresh surfaces, where weathering was minimum and no vegetation had developed on the fault plane. For these surfaces, the data recovery was excellent, greater than 99.5%. We therefore obtained the topography of the surfaces without holes in the data, making the signal processing results reliable.

6. Roughness results and interpretation

6.1 Magnola Fault

The roughness analysis results of the Magnola fault outcrop and hand sample are shown on Figure 11. On each plot (Figure 11a-d) both Lidar data (upper curve), acquired with the Optech scanner (Table 2), and laboratory profilometer data (lower curve) are represented, showing a scaling behavior over 5.5 orders of magnitude of length scales (50 μm to approximately 20 m). Each curve represents an average over a large set of parallel 1D profiles

extracted from the DEM of the fault surface shown on Figure 9. The level of noise for the field LIDAR scanner (Table 1) is estimated as the height of the flat part of the spectrum at small length scales and is indicated by the black arrows (Figure 11). The flattening of the scaling behavior at large scales is related to a finite size effect.

The FPS and WPS techniques performed along and perpendicular to the slip direction (Figure 11a-d) indicate that the power laws can easily be connected for the field and laboratory data, demonstrating the robustness of the scaling behavior. Moreover, our results highlight a significant directional morphological anisotropy over a wide range of scales: the profiles parallel to the slip direction are rougher than perpendicular ones (POWER *et al.*, 1988; POWER and TULLIS, 1991; LEE and BRUHN, 1996; POWER and DURHAM, 1997; RENARD *et al.*, 2006; SAGY *et al.*, 2007). These two methods estimate a similar Hurst exponent perpendicular to the slip orientation ($H_{\perp} = 0.8$) across the whole range of scales investigated in this study, a property similar to fresh mode I fracture surfaces (POWER *et al.*, 1987; SCHMITTBUHL *et al.*, 1995b, BOUCHAUD, 1997). However, the FPS technique indicates a greater anisotropy, $\left|H_{//} - H_{\perp}\right| = 0.2$, where $H_{//}$ represents the Hurst exponent in the direction of slip, than quantified by the WPS method ($\left|H_{//} - H_{\perp}\right| = 0.1$). Moreover, the WPS method overestimates the self-affine exponent along the slip direction ($H_{//} = 0.7$) compared to the FPS method ($H_{//} = 0.6$). An attempted explanation of these last two differences is given by our parametric study of synthetic rough surfaces: the WPS method slightly overestimates the roughness exponents when measuring couples of Hurst exponents in perpendicular directions with range of values similar to those of natural fault surface (0.6 to 0.9). Notably, the exponents accuracy with anisotropic surface of 2049 x 2049 points and for two Hurst exponents in perpendicular direction of 0.8 and 0.6 is numerically estimated as -0.01 and -0.06 for the wavelet method, respectively (Figure 4f). For example, an amount of -0.06 should be added to the measured minimal exponent with the WPS analysis to obtain the

490 actual one. Accordingly, on natural fault surface with two perpendicular exponents of 0.8 and
491 0.6 calculated by the FPS, the estimated Hurst exponent in direction parallel to slip is
492 systematically lower than with the WPS method (Figures 11-12). Moreover, since the error on
493 the output Hurst exponent is greater in direction of slip than perpendicularly to it,
494 consequently the output anisotropy decreases, as observed on natural fault surface (Figure 11-
495 12).
496 Our estimations obtained on the hand sample with the RMS-COR function (see Figure 11e)
497 show that the minimum Hurst exponent ($H = 0.6$) is at 85°, in the direction of slip, and the
498 maximum Hurst exponent ($H = 0.8$) is almost in the perpendicular direction. These two
499 extremes values of the self-affine exponent correspond also to those determined at all scales
500 by the FPS and WPS methods. At the field scale (see Figure 11e), the minimum ($H = 0.4$)
501 and maximum ($H = 0.7$) Hurst exponents are observed in directions similar to that for the
502 hand sample. However, the results obtained with the RMS-COR method suggest that the
503 roughness exponent of the Magnola fault surface is smaller at the field scale compared to the
504 laboratory scale, regardless of the azimuth. We ascribe this variation to natural weathering
505 (pitting) of the exposed fault surface at short wavelengths, as POWER and TULLIS (1991).
506 Indeed, the section of the Magnola fault surface (Figure 9a) shows an increase of the
507 roughness amplitude at short wavelengths created by weathering. Other sections of the
508 Magnola fault surface, that are not presented in this study, display evidence of strong
509 alteration at short length scales leading to a significant reduction of the Hurst exponent,
510 regardless of azimuth. Conversely, the clean hand sample (Figure 9b), that shows mechanical
511 striations, should represent the actual topography of the fault surface at short length scales,
512 related to the faulting process before the action of climatic weathering. This hypothesis is
513 supported by the fact that the fresh slip plane, scanned in laboratory, displays the same self-
514 affine RMS-COR regimes in the directions parallel and perpendicular to slip than those

estimated using the FPS and WPS methods. The increase of roughness at short wavelengths on the field surface due to the erosion appears to be similar to the effect of an additional noise tested on “ideal” synthetic surfaces (Figure 7). In both cases, the Hurst exponent decreases in all directions. Our statistical study led on synthetic surfaces shows that the noise effect is more pronounced when using the RMS-COR technique. To summarize, the roughness scaling estimated using the RMS-COR calculated on the weathered field surface exhibits a decrease of the Hurst exponent in all directions, which is not observed with the FPS and WPS techniques.

On the polar plot of H obtained at the laboratory scale (see Figure 11e), when departing a few degrees from the direction of slip, the Hurst exponent is close to the value of the maximum Hurst exponent measured in the direction perpendicular to mechanical striations. Such behavior is also visible on ‘ideal” synthetic surfaces (Figure 5). In other words, the azimuth of the maximum Hurst exponent is not well-defined (gray shadows on Figure 11e), while the minimum exponent corresponds to a specific orientation. Note that this property is less visible on the polar plot of the altered field fault section (see Figure 11e) where the angular variation of H is more progressive.

6.2 Vuache Fault

The FPS and WPS techniques highlight a significant directional morphological anisotropy over six orders of spatial scales (Figure 12a-d). Profiles parallel to slip have a smaller Hurst exponent than perpendicular ones (POWER *et al.*, 1988; POWER and TULLIS, 1991; LEE and BRUHN, 1996; POWER and DURHAM, 1997; RENARD *et al.*, 2006; SAGY *et al.*, 2007). These two methods, applied to series of profiles perpendicular to the direction of slip, indicate that the power laws of individual surfaces can easily be connected across the wide range of scales investigated (Figure 12b, d), and the value of $H_{\perp} = 0.8$ is similar to what was measured on the Magnola normal fault surface. However, in the slip parallel direction there is

a slight change in the magnitude of $H_{//}$ located in the length scale range between 5 mm and 2 cm (gray shadows on Figure 12a, c). $H_{//} = 0.75$ is larger below this length scale range than at larger length scales, where $H_{//} = 0.65$ and $H_{//} = 0.7$ for the FPS and WPS methods, respectively. The smoother aspect of the Vuache fault surface in the direction of slip compared to the perpendicular direction is an obvious and expected consequence of striations, but the smallest directional morphological anisotropy at the laboratory scale compared to the field scale is novel in this study. At the field scale, the morphology of the elongated bumps and depressions along the slip direction is different from the grooves and striations observed at the laboratory scale (Figure 10). As the fault Vuache outcrop is quite fresh, and was preserved from the climatic erosion, we propose that this cross-over in the slope at length scale of several millimeters is significant. We interpret this cross-over length scale as a witness of different mechanical processes responsible for the creation of fault topography at different spatial scales.

Our results obtained at the field and intermediate scales with the RMS-COR function (see left and center plots on Figure 12e) show that the minimum Hurst exponent ($H_{//} \in [0.55-0.6]$) is oriented at 20° with respect to the horizontal, indicating the fault had a normal component and not only a strike-slip one. The maximum value $H = 0.75$ is located for an almost perpendicular direction. These two extremes values of the self-affine exponent are slightly lower when estimated using the RMS-COR function than when using the FPS or the WPS methods. This slight underestimation with the RMS-COR technique is consistent with our results on synthetic surfaces for the accuracy in this range of parameters (Figure 4). Indeed, our parametric study led on anisotropic synthetic surfaces shows that the estimation of H calculated with the RMS-COR technique slightly underestimates its actual value (Figure 4d). At the laboratory scale (see right plot on Figure 12e), $H_{//} = 0.8$ and $H_{\perp} = 0.9$ are located in orientations similar to that for the three larger surfaces measured on the field. However, the

polar plot of H calculated using the RMS-COR function suggests an increase of the scaling exponents in all directions, while the estimation using the FPS or WPS techniques underlined that the exponent increased only along the slip direction. In addition, the two exponents $H_{//}$ and $H_{\perp}$ for the hand sample are overestimated when calculated with the RMS-COR method compared to the FPS and WPS techniques. The latter observation cannot be explained by the results of our parametric study on synthetic surfaces. As a consequence of the extremely smooth aspect of the hand sample at small scales (Figure 10f), the RMS-COR method could lose its robustness. However, a new reliable result is that the directional morphological anisotropy calculated by the RMS-COR function significantly decreases at the laboratory scale, as observed with the FPS and WPS techniques.

As already observed on the polar plot of H calculated on the Magnola fault surface (Figure 11e), the azimuth of the maximum Hurst exponent is less constrained (gray shadows on Figure 12e) than the single specific orientation of the striations. Remarkably, despite the weak anisotropy of the hand sample topography, the slip direction is always significant, demonstrating the accuracy and reliability of the RMS-COR method.

7. Discussion & Conclusion

The six statistical tools used in this study have different response under the effect of two kinds of biases, the intrinsic errors of the methods (Figures 3, 4, 5, 6) and the artifacts inherent in data acquisition (Figures 7, 8). Using a parametric approach, where we varied the size of the surface and its anisotropy, we selected the three most reliable and accurate methods (RMS-COR, FPS, WPS) for roughness analysis of natural fault topography (Figures 11, 12). The Hurst exponent estimation at various scales for the natural slip surfaces displays the same trends and provides a consistent and robust characterization of their scaling regimes. We

589 emphasize that the slight variations in the results given by each one of these methods fall
590 within the range of error estimated by our parametric study (see Section 4).
591 One of the most robust results of our scaling analysis is that the FPS and the WPS methods
592 estimate a same Hurst exponent equal to 0.8 in the direction perpendicular to slip, over
593 approximately 6 orders of magnitude of length scales for two different fault surfaces (Figures
594 11b, d and 12b, d). However, in the slip direction two different scaling behaviors are
595 highlighted: the Magnola fault surface shows an identical scaling regime at large and small
596 scales (Figure 11a, c). Conversely, the scaling property of the Vuache fault roughness exhibits
597 a cross-over in the slope at length scale of several millimeters (Figure 12a, c). In other words,
598 the scaling property of this fault surfaces is similar at large scales but changes at small scales.
599 The statistical analyses (Figure 12) and the scan of the Vuache fault surface (Figure 10)
600 clearly show a smoothing of the roughness below a length scale of several millimeters.
601 The scaling regime of 0.8 measured in the direction perpendicular to slip is a classical result
602 already observed for tensile cracks (POWER *et al.*, 1987; SCHMITTBUHL *et al.*, 1995b,
603 BOUCHAUD, 1997), indicating that the topography of the fault surface in the direction
604 perpendicular to slip has not registered the effect of shear. Along slip, the general
605 interpretation is that mechanical wear processes, such as frictional ploughing, cause striations
606 that reduce the amplitude of the large scale roughness (POWER *et al.*, 1987, 1988; POWER
607 and TULLIS, 1991; POWER and DURHAM, 1997; SAGY *et al.*, 2007) and accordingly the
608 Hurst exponent. Nevertheless, our scaling analysis seems to indicate different mechanical
609 processes responsible for the creation of fault topography at different spatial scales.
610 Prior comparative studies of natural fault roughness based on 1D profilometry (POWER and
611 TULLIS, 1991; LEE and BRUHN, 1996) suggest a change in scaling properties between large
612 and short length scales. However, due to technical limitations, their measures were not

613 sufficiently accurate to decipher if this variation was related either to small-scale surface
614 weathering of the fault scarp or to the faulting process itself.
615 From laboratory experiments CHEN and SPETZLER (1993) suggest that the break in slope at
616 length scales of several millimeters is caused by a change in the dominant mode of
617 deformation from small-scale intergranular cracking to intragranular cracking at a larger
618 scale. We think this interpretation does not apply to the Magnola and Vuache faults because
619 the grain scale of these limestones is very small (< 0.1mm), well below the observed cross-
620 over length scale.
621 Recently, SAGY *et al.* (2007) observed that faults with large cumulated slip display surfaces
622 with elongate, quasi elliptical bumps at field scale and are polished at small scales.
623 Conversely, fault with a small cumulative slip are rough on all scales. SAGY and BRODSKY
624 (2008) proposed that the waviness of the large slip fault surface reflects variations of
625 thickness of the cohesive layer under the slip surface formed as boudinage structures
626 (JOHNSON and FLETCHER, 1994; SMITH, 1977; TWISS and MOORES, 1992,
627 GOSCOMBE *et al*., 2004). Therefore, they evoke two different deformation mechanisms
628 between large and small scales: abrasion caused by frictional sliding at the origin of the
629 smoothing at small scales, and “boudinage” creating elongated bumps and depression at large
630 scales.
631 From our study of natural fault roughness, we observe large elongated bumps and depressions
632 in slip direction on two different fault planes (Figures 9b, 10a-d). There is no evidence that
633 the small segment, polished at small scale (Figure 10f), that connects to the main Vuache fault
634 has accumulated more slip than the Magnola fault surface that is rough at all scales (Figure
635 9b, c). Therefore, we propose that large elongated bumps and depressions of several meters in
636 length with maximum amplitude of around 2 m may reflect the processes of lateral growth
637 and branching that links together several fault surfaces, during all the stages of the evolution

of the fault zone, as suggested by LEE and BRUHN (1996) and LIBICKI and BEN-ZION (2005).

At small scales, two different kinds of scaling regime are observed on the two fault surfaces, (Figures 11, 12), both being linked to mechanical wear process. Frictional sliding is expressed through ploughing of small asperities and is responsible for the small scale abrasional striations on the Magnola fault surface (Figure 9c). This mechanism is also responsible for the polishing of the Vuache fault surface below the centimeter scale (Figure 10f). One should keep in mind that only one hand sample was measured for each surface and therefore it is possible that differences of the scaling behavior between the two fault planes reflect spatial heterogeneity of core fault at small scales. Notably, on the Vuache fault, although the surface appears polished at the laboratory scale on the whole surface, zones with striations due to ploughing elements could be present. A more extensive study of fault roughness in several different faults should therefore bring more information on the mechanisms at work during faulting.

References

AMITRANO, D. and SCHMITTBUHL, J. (2002), *Fracture roughness and gouge distribution of a granite shear band*, J. Geophys. Res. *107*(B12), 2375, doi: 10.1029/2002JB001761.

AKI, K. (1984), *Asperities, barriers, characteristic earthquakes and strong motion prediction*, J. Geophys. Res. *89*, p. 5867–5872.

BARABASI, A.-L. and STANLEY, H.E. (1995), *Fractal Concepts in Surface Growth*, Cambridge University Press.

BIERME, H., MEERSCHAERT, M. M., and SCHEFFLER, H.-P. (2007), *Operator scaling stable random fields*, Stoch. Proc. Appl. *117*, 312-332.

BIERME, H., BROUSTE, A., and LACAUX, C. (2008), *Generalized quadratic variations for operator scaling Gaussian random fields*, preprint.

BEN-ZION, Y. and SAMMIS, C.G. (2003), *Characterization of fault zones*, Pure and Appl. Geophys. *160*, p. 677–715, doi: 10.1007/PL00012554.

BOUCHAUD, E. (1997), *Scaling properties of cracks*, J. Phys. Condens. Matter, 9, 4319–4344.

BROWN, S.R. and SCHOLZ, C.H. (1985), *Broad bandwidth study of the topography of natural rock surfaces*, J. Geophys. Res. *90*, p. 2575–2582.

688 CAMPILLO, M., FAVREAU, P., IONESCU, I.R., and VOISIN, C. (2001), *On the effective*
689 *friction law of an heterogeneous fault*, J. Geophys. Res. *106*, p.307-322.
690
691 CARCAILLET, J., MANIGHETTI, I., CHAUVEL, C., SCHLAGENHAUF, A., and
692 NICOLE, J. M. (2008), *Identifying past earthquakes on an active normal fault (Magnola,*
693 *Italy) from the chemical analysis of its exhumed carbonate fault plane*, Earth Planet. Sci. Lett.
694 *271*, 145-158, doi:10.1016/j.epsl.2008.03.059.
695
696 CHEN, G. and SPETZLER, H. A. (1993), *Topographic characteristics of laboratory-induced*
697 *shear fractures*, Pure and Appl. Geophys. *140*, p. 123–135.
698
699 GOSCOMBE, B. D., PASSCHIER, C., and HANDA, M. (2004), *Boudinage classification:*
700 *end-member boudin types and modified boudin structures*, J. Struct. Geol. *26*, 739–763.
701
702 JOHNSON, A. M. and FLETCHER, R. C. (1994), *Folding of Viscous Layers: Mechanical*
703 *Analysis and Interpretation of Structures in Deformed Rock*, Columbia University Press.
704
705 LAY, T., KANAMORI, H., and RUFF. (1982), *The asperity model and the nature of large*
706 *subduction zone earthquakes*, Earthquake Prediction Research, *1*, p. 3–71.
707
708 LEE, J.-J. and BRUHN, R. (1996), *Structural anisotropy of normal fault surfaces*, J. Struct.
709 Geol. *18*, 1043– 1059.
710

LIBICKI, E. and BEN-ZION, Y. (2005), *Stochastic Branching Models of Fault Surfaces and Estimated Fractal Dimensions*, Pure and Appl. Geophys. *162*, 1077-1111, doi: 10.1007/s00024-004-2662-7.

MANDELBROT, B. B. (1985), *Self-affine fractals and fractal dimension*, Phys. Scripta. *32*, 257-260.

MARSAN, D. (2006), *Can coseismic stress variability suppress seismicity shadows ? Insights from a rate-and-state friction model*, J. Geophys. Res. *111*, B06305, doi:10.1029/2005JB004060.

MANDELBROT, B.B. (1986), *Fractals in Physics*, Elsevier, Amsterdam.

MEAKIN, P. (1998), *Fractals: Scaling and Growth Far From Equilibrium*, Cambridge Univ. Press, New York.

MEHEUST, Y. (2002), *Ecoulements dans les fractures ouvertes*, Ph. D. Thesis, Univ. Paris VI & Ecole Normale Supérieure, Paris.

OKUBO, P. G. and AKI, K. (1987), *Fractal Geometry in the San Andreas Fault System*, J. Geophys. Res. *92*, 345–355.

PALUMBO, L., BENEDETTI, L., BOURLES, D., CINQUE, A., and FINKEL, R. (2004), *Slip history of the Magnola fault (Apennines, Central Italy) from ^{36}Cl surface exposure*

dating: evidence for strong earthquakes over the Holocene, Earth Planet. Sci. Lett. *225*, 163-176.

PARSONS, T. (2008), *Persistent earthquake clusters and gaps from slip on irregular faults,* Nature Geoscience, *1*, p. 59-63, doi:10.1038/ngeo.2007.36.

PEYRAT, S., OLSEN, K.B., MADARIAGA, R. (2004), *Which Dynamic Rupture Parameters Can Be Estimated from Strong Ground Motion and Geodetic Data?*, Pure and Appl. Geophys. *161*, p. 2155–2169, doi: 10.1007/s00024-004-2555-9.

POWER, W.L., TULLIS, T.E., and WEEKS, J.D. (1988), *Roughness and wear during brittle faulting*, J. Geophys. Res. *93*, p. 15,268–15,278.

POWER, W. L., TULLIS, T. E., BROWN, S. R., BOITNOTT, G. N., and SCHOLZ, C. H. (1987), *Roughness of natural fault surfaces*, Geophys. Res. Lett. *14*, 29–32.

POWER, W. L. and TULLIS, T. E. (1991), *Euclidean and Fractal Models for the Description of Rock Surface Roughness*, J. Geophys. Res. *96*, 415–424.

POWER, W. L. and DURHAM, W. B. (1997), *Topography of natural and artificial fractures in granitic rocks: Implications for studies of rock friction and fluid migration*, Int. J. Rock Mech. Min. Sci. *34*, 979–989.

RENARD, F., VOISIN, C., MARSAN, D., and SCHMITTBUHL, J. (2006), *High resolution 3D laser scanner measurements of a strike-slip fault quantify its morphological anisotropy at all scales*, Geophys. Res. Lett. *33*, L04305, doi: 10.1029/2005GL025038.

RUBIN, A. M., GILLARD, D., and GOT, J.-L. (1999), *Streaks of Microearthquakes along Creeping Faults*, Nature, *400*, 635–641.

SAGY A., BRODSKY, E. E., and AXEN, G. J. (2007), *Evolution of fault-surface roughness with slip*, Geology, *35*, 283-286.

SAGY, A. and BRODSKY, E. E. (2008), *Geometric and Rheological Asperities in an Exposed Fault Zone*, preprint to J. Geophys. Res.

SCHAFF, D. P., BOKELMANN, G. H. R., BEROZA, G. C., WALDHAUSER, F., and ELLSWORTH, W. L. (2002), *High-resolution image of Calaveras Fault seismicity*, J. Geophys. Res. *107*(B9), 2186, doi:10.1029/2001JB000633.

SCHMITTBUHL, J., CHAMBON, G., HANSEN, A., and BOUCHON, M. (2006), *Are stress distributions along faults the signature of asperity squeeze?*, Geophys. Res. Lett. *33*, L13307, doi:10.1029/2006GL025952.

SCHMITTBUHL, J., GENTIER, S., and ROUX, R. (1993), *Field measurements of the roughness of fault surfaces*, Geophys. Res. Lett. *20*, 639– 641.

SCHMITTBUHL, J., VILOTTE, J., and ROUX, S. (1995a), *Reliability of self-affine measurements*, Phys. Rev. E. *51*, 131– 147.

SCHMITTBUHL, J., SCHMITT, F., and SCHOLZ, C. (1995b), *Scaling invariance of crack surfaces*, J. Geophys. Res. *100*, 5953–5973.

SCHOLZ, C. H. (2002), *The Mechanics of Earthquake and Faulting*, Cambridge Univ. Press, New York.

SIMONSEN, I., HANSEN, A., and NES, O. M. (1998), *Using wavelet transforms for Hurst exponent determination*, Phys. Rev. E. *58*, 2779–2787.

SMITH, R. B. (1977), *Formation of folds, boudinage, and mullions in non-Newtonian materials*, Geol. Soc. Amer. Bull. *88*, 312-320.

STEIN, M. L. (2002), *Fast and exact simulation of fractional Brownian sufaces*, J. Comput. Graph. Statist. *11*, 587-599.

THOUVENOT, F. (1998), *The ML 5.3 Epagny (French Alps) earthquake of 1996 July 15: A long-awaited event on the Vuache Fault*, Geophys. J. Int. *135*, 876– 892.

TWISS, R. J. and MOORES, E. M. (1992), *Structural Geology*, W. H. Freeman, New York.

VOISIN, C., CAMPILLO, M., IONESCU, I., HASSANI, R., and NGUYEN, Q.-L. (2002a), *Process and signature of initiation on a finite fault system: a spectral approach*, Geophys. J. Int. *148*, 120– 131.

VOISIN, C., IONESCU, I., CAMPILLO, M. (2002b), *Crack growth resistance and dynamic rupture arrest under slip dependent friction*, Physics of the Earth and Planetary Interiors, *131*, 279-294.

VOSS, R.F. (1985), *Scaling Phenomena in Disorder Systems*, Plenum, New York.

815 Table 1: Characteristics of the field and laboratory scanner devices.

3D scanner device	S10	GS100	LMS Z420i	Ilris-3D	Lab. Profilometer
Company	Trimble	Trimble	Riegl	Optech	Univ. Strasbourg
Resolution (dx)	0.5 mm	10 or 20 mm	20 mm	20 mm	20 or 24 μm
Noise on the data	0.9 mm	4.5 mm	10.2 mm	20 mm	< 1 μm
Acquisition speed	70 pts/s	5000 pts/s	5000 pts/s	2500 pts/s	60 pts/s

816

817 Table 2: Fault surfaces analyzed in this study.

Fault	**Surface area, dx**	**Scanner**
Vuache, SURF1	17 x 10 m, 20 mm	GS100
Vuache, SURF7	24 x 11 m, 30 mm	GS100
Vuache, SURF6	45 x 9 m, 20 mm	LMS Z420i
Vuache, SMALL	10 x 9 cm, 24 μm	Lab. Profilometer
Vuache, SURF-JPG	0.5 x 0.5 m, 1 mm	S10
Magnola, A32	35 x 15 m, 20 mm	Optech
Magnola, M2	7.2 x 4.5 cm, 20 μm	Lab. Profilometer

818

```
function RoughSurf = Synthetic2DFault(N,H1,H2)

% This Matlab(c) function creates a self-affine 2D surface,
% with a directional anisotropy (courtesy of Hermine Bierme,
% Univ. Paris V, France), when H1 is different from H2.
% Input parameters:
% N = size of the surface: (2^(N+1)+1) x (2^(N+1=+1)
% Typically N must be between 8 and 11 when running on a
desktop computer.
% H1, H2: Hurst exponents in two perpendicular directions
% must be positive, smaller than 1.
% Output result:
% RoughSurf: rough surface of size (2^(N+1)+1) x (2^(N+1=+1),
% with two perpendicular directions of self-affinity
% characterized by Hurst exponents H1 and H2, l1 = 1/H1 and
% l2 = 1/H2 represent the eigen values of the anisotropy
% diagonal matrix
l1 = 1/H1;
l2 = 1/H2;
X = (-2*2^N:2:2*2^N)/(2^(N+1));
X(2^N+1) = 1/2^N;
Y = (-2*2^N:2:2*2^N)/(2^(N+1));
Y(2^N+1) = 1/2^N;
XX = X(ones(1,2*2^N+1),:);
YY = Y(ones(1,2*2^N+1),:)';
clear X Y

% rho is the pseudo-norm associated to the eigen values l1 and
l2
% rho(x,y)=(abs(x)^(2/l1) + abs(y)^(2/l2) )^(1/2)
rho = sqrt(abs(XX).^(2/l1)+abs(YY).^(2/l2));
clear XX YY

%phi is the spectral density of the field built from rho
phi = rho.^(1 + (l1+l2)/2);
clear rho

% W = Fourier transform of the anisotropic Gaussian field
Z = randn(2*2^N+1,2*2^N+1);
W = fftshift(fft2(Z))./phi;
clear Z
T = real(ifft2(ifftshift(W)));
RoughSurf = T-T(2^N+1,2^N+1);

% Plot the 2D rough surface
imagesc(RoughSurf);
axis equal
axis tight


```

Figures and Captions

Figure 1. Digital Elevation Models (DEM) of 2D synthetic self-affine surfaces (up) and 1D profiles (down) generated using the algorithm of the appendix. (a) Surface with an isotropic self-affine property characterized by a Hurst exponent of 0.8. (b) Anisotropic self-affine surface with two Hurst exponents ($H_{//} = 0.6$ and $H_{\perp} = 0.8$) in perpendicular directions. (c) Representative 1D profiles extracted in two perpendicular directions of surface (b). Inset: magnified portion of a profile along the $H_{//}$ direction (parallel to the striations), which has a statistically similar appearance to the entire profile when using a rescaling $\delta x \rightarrow \lambda\, \delta x$, $\delta z \rightarrow \lambda^{H} \delta z$.

Figure 2. Outputs of the six signal processing techniques applied on the data of the anisotropic self-affine surface shown in Figure 1b. (a) Root-mean-square correlation (RMS), (b) maximum-minimum height difference (MM), (c) correlation function (COR), (d) RMS correlation function (RMS-COR), (e) Fourier power spectrum (FPS), (f) Wavelet power spectrum (WPS). The inset in (d) displays a polar plot of H obtained by the RMS-COR method and allowing then to determine the azimuth dependence of H. The black points correspond to the Hurst exponents for the two profiles shown on this plot.

Figure 3. Comparisons between the "input" Hurst exponents introduced in the construction of isotropic fractional Brownian surfaces and the "output" exponent measured on these surfaces using the six independent signal processing techniques. The effect of system size is also studied. (a) Root-mean-square correlation (RMS), (b) maximum-minimum height difference (MM), (c) correlation function (COR), (d) RMS correlation function (RMS-COR), (e) Fourier

power spectrum (FPS), (f) Wavelet power spectrum (WPS). The gray line in (a), (b), and (c) indicate for which input exponent the error in the estimation is closest to zero.

Figure 4. Intrinsic errors in the estimation of the Hurst exponents for anisotropic synthetic surfaces characterized by two Hurst exponents $H_{input\,//}$ and $H_{input\perp}$ in perpendicular directions (2049x2049 points, similar to Figure 1b). For each signal processing method, histogram plots are represented where the horizontal axis contains the Hurst exponents $H_{input\,//}$ and $H_{input\perp}$ used as inputs to generate the synthetic surface. The vertical axis represents the difference between the input exponent and the estimated output Hurst exponent, using the six different methods. For each method, two histogram plots are represented: the upper one shows the difference ($H_{input\,//} - H_{output\,//}$) and the lower one the difference ($H_{input\perp} - H_{output\perp}$). The black top surfaces on the histogram bars indicate a negative difference (overestimation of the output exponent) and the color ones a positive difference (underestimation of the output exponent). (a) Root-mean-square correlation (RMS), (b) maximum-minimum height difference (MM), (c) correlation function (COR), (d) RMS correlation function (RMS-COR), (e) Fourier power spectrum (FPS), (f) Wavelet power spectrum (WPS).

Figure 5. Polar plots of the angular dependence of the two Hurst exponents $H_{//}$ and $H_{\perp}$ for synthetic anisotropic surfaces with principal directions oriented at angles $\theta_{//} = 0°$ and $\theta_{\perp} = 90°$. The Hurst exponents $H_{//,\perp}(\theta)$, as defined by the slope $\beta = H$ in Figure 2d, were calculated on series of 1D profiles extracted at an angle θ on 2049x2049 points surfaces. Three series of simulations are represented here for three values of $H_{//}$ in the range [0.7 – 0.9]. For each polar plot, the different curves corresponds to successive values of $H_{\perp}$. The

dashed lines correspond to the values of the output Hurst exponent measured with the RMS correlation method (center dashed circle: $H = 0.2$, outer dashed circle: $H = 1$).

Figure 6. Quantification of the intrinsic errors on the estimation of the anisotropy of the surface ($H_{//} - H_{\perp}$). The difference between the "input" anisotropy (difference between the two "input" Hurst exponents) introduced in synthetic surfaces (2049x2049 points, similar to Figure 1b), minus the "output" anisotropy is represented for the six signal processing methods: (a) Root-mean-square correlation (RMS), (b) maximum-minimum height difference (MM), (c) correlation function (COR), (d) RMS correlation function (RMS-COR), (e) Fourier power spectrum (FPS), (f) Wavelet power spectrum (WPS). Bars with black top surface indicate an overestimation ("input" anisotropy - "ouput" anisotropy < 0) and colored top surfaces indicate an underestimation ("input" anisotropy - "ouput" anisotropy > 0). Gray bars indicate isotropic surfaces ($H_{//} = H_{\perp}$), thus without errors.

Figure 7. Influence of an additional noise on the self-affinity property of an anisotropic synthetic surface (513x513 points) characterized by two Hurst exponents ($H_{//} = 0.6$ and $H_{\perp} = 0.8$) in perpendicular directions. The Gaussian white noise is characterized by a standard deviation two hundred times smaller than the roughness amplitude of the synthetic surface. (a) Example of 1D profiles extracted in two perpendicular directions of an "ideal" surface. (b) The same profiles but with an additional noise. Note that altered profiles appear more jagged or rougher at small scale compared the noise-free profiles. Analyses of those altered surfaces are performed with the six independent self-affine methods: (c) Root-mean-square correlation (RMS), (d) maximum-minimum height difference (MM), (e) correlation function (COR), (f) RMS correlation function (RMS-COR), (g) Fourier power spectrum (FPS), (h) Wavelet power spectrum (WPS). For each method, except the RMS-COR function,

two plots are represented: the upper plot shows the difference between the noise-free surface and the altered surfaces in the direction of the largest exponent and the lower one in direction of the smallest exponent. For the RMS-COR technique, the upper plot represents the difference between the noise-free and the altered surface in both directions: perpendicular and parallel to striations. The lower subplot displays two polar plot of H obtained with the noise-free and the biased surfaces. Note that the flattening of the scaling behavior at large scales is related to a finite size effect.

Figure 8. Influence of the interpolation of missing data on the estimation of the Hurst exponent. (a) Synthetic surface (513x513points) with H = 0.8. (b) Same surface with 5% of holes (white dashed lines) that have been interpolated. c) 3D view of the surface in a) with the holes. (d) RMS correlation function (RMS-COR), (e) Fourier power spectrum (FPS), (f) Wavelet power spectrum (WPS). The different curves on each plot present the result of the analysis for five different percentages of missing points (5%, 10%, 20%, 40%).

Figure 9. 3D scanner data of the Magnola fault slip surface at different scales. (a) Photograph of the fault surface, showing significant weathering and covering by vegetation. The black polygon corresponds to the surface shown below. (b) Digital Elevation Model (DEM) of the surface A32 (Table 2). The LIDAR data contain 799,830 points, sampled on a roughly regular grid of ~40 x ~40 mm. The measurements were performed on a ~20 x ~20 mm grid and then averaged on a coarser grid. The resolution of the elevation is 20 mm. The fault surface shows elongated bumps (red) and depressions (blue), dipping at approximately 85°, and indicating a main normal slip motion. The corrugation, with maximum amplitude of around 2.2 m, can be observed at all scales down to the measurement resolution. (c) DEM of hand sample M2 (Table 2) that contains 3999 x 3120 points on a regular mesh of 20 x 20 μm^2. The surface

contains grooves (blue) and ridges (red) aligned parallel to slip and with maximum amplitude of around 1.2 mm.

Figure 10. 3D data of the Vuache fault slip surface at all scales. (a) Photograph of the outcrop, where the white boxes correspond to the surfaces shown in (c) and (d). (b) Lateral photograph of the slip plane that highlights its remarkable waviness. (c-d) Fault surface topography of SURF1 and SURF6 (Table 2). Each surface contains approximately 450,000 points sampled on a constant grid of 20 x 20 mm. The resolution of the elevation is 10.2 mm for (c) and 4.5 mm for (d), respectively. The surfaces show large elongated bumps (red) and depressions (blue) with maximum amplitude of around 2 m associated with linear striations of smaller size (grooves and ridges). Both geometrical patterns dipping at 15-25° indicate a strike-slip motion with a small normal component. (e) DEM of the bumpy zone SURF-JPG (Table 2) that contains 107,606 points sampled on a regular grid of 1 x 1 mm. Note the vertical exaggeration. The resolution of the elevation is 0.9 mm. (f) DEM of the hand sample SMALL (Table 2) that contains 4099 x 3333 points on constant grid of 24 x 24 μm^2. The resolution of the elevation is less than one micrometer. The scans clearly show a smoothing of the roughness from large to small scales. Large fault surface measured on the field have asperities over the entire range of observed scales down to the measurement resolution. Conversely, the laboratory data show that the surface below the centimeter scale appears more polished and only smooth decimeter ridges persist.

Figure 11. Roughness scaling analysis from the best preserved outcrops of the Magnola fault plane, scanned using ground based LIDAR (surface A32, Figure 9b), or using the laboratory profilometer (hand sample M2, Figure 9c). (a-b) Fourier Power Spectrum (FPS), and (c-d) Wavelet power spectrum (WPS) along two directions, parallel and perpendicular to the

992 direction of slip, are represented in log-log plots. Power-law fits (black dotted line) are
993 performed for each curve and the corresponding slopes (β) and roughness exponents (H) are
994 indicated above the spectra. The inset displays an example of the amplitude (Z) and the
995 wavelength (λ) of a rough profile. Contours (red lines) of constant amplitude (Z) to
996 wavelength (λ) ratio, reflecting a self-similar behavior, are provided to allow easier
997 interpretation of the spectra. Black arrows indicate the level of noise of the LIDAR. (e)
998 Surface anisotropy revealed by the angular variation of the Hurst exponent determined by the
999 RMS correlation function method. The polar plot of H on the left and the right sides
1000 correspond to data of the field surface and hand sample shown on Figure 9, respectively.
1001
1002 **Figure 12.** Roughness scaling analysis from five surfaces (Figure 10, Table 2) of the Vuache
1003 fault, covering 6 orders of magnitude of frequencies or wavelengths (40 μm to approximately
1004 40 m). The data collected contain four surfaces (blue and green curves) that have been
1005 scanned using LIDAR and one hand sample (magenta curve) measured by laboratory
1006 profilometer. (a-b) Fourier power spectrum (FPS) and (c-d) Wavelet power spectrum (WPS)
1007 along two directions, parallel and perpendicular to the direction of slip, are represented in log-
1008 log plots. Power law fits (black dotted line) are shown for each curve and the corresponding
1009 slopes (β) and roughness exponents (H) are indicated next to the spectra. Each curve is an
1010 average over a series of parallel profiles extracted from the DEM shown on Figure 10. The
1011 level of noise for the Lidar scanners is estimated as the height of the flat part of the spectrum
1012 at small length scales and is indicated by the black arrows. The flattening of the scaling
1013 behavior at large scales is related to a finite size effect. Contours (red lines) of constant
1014 amplitude (Z) to wavelength (λ) ratio, reflecting a self similar surface, are also indicated a
1015 guide for the eye. The inset displays an example of the amplitude (Z) and the wavelength
1016 (λ) of a rough profile. (e) Roughness anisotropy revealed by the angular variation of the

1017 Hurst exponent determined by the RMS-COR method. The polar plots of H on the left, in the
1018 center and on the right correspond to data of the field surface, the intermediate scale section
1019 and hand sample, respectively (see Figure 10).
1020

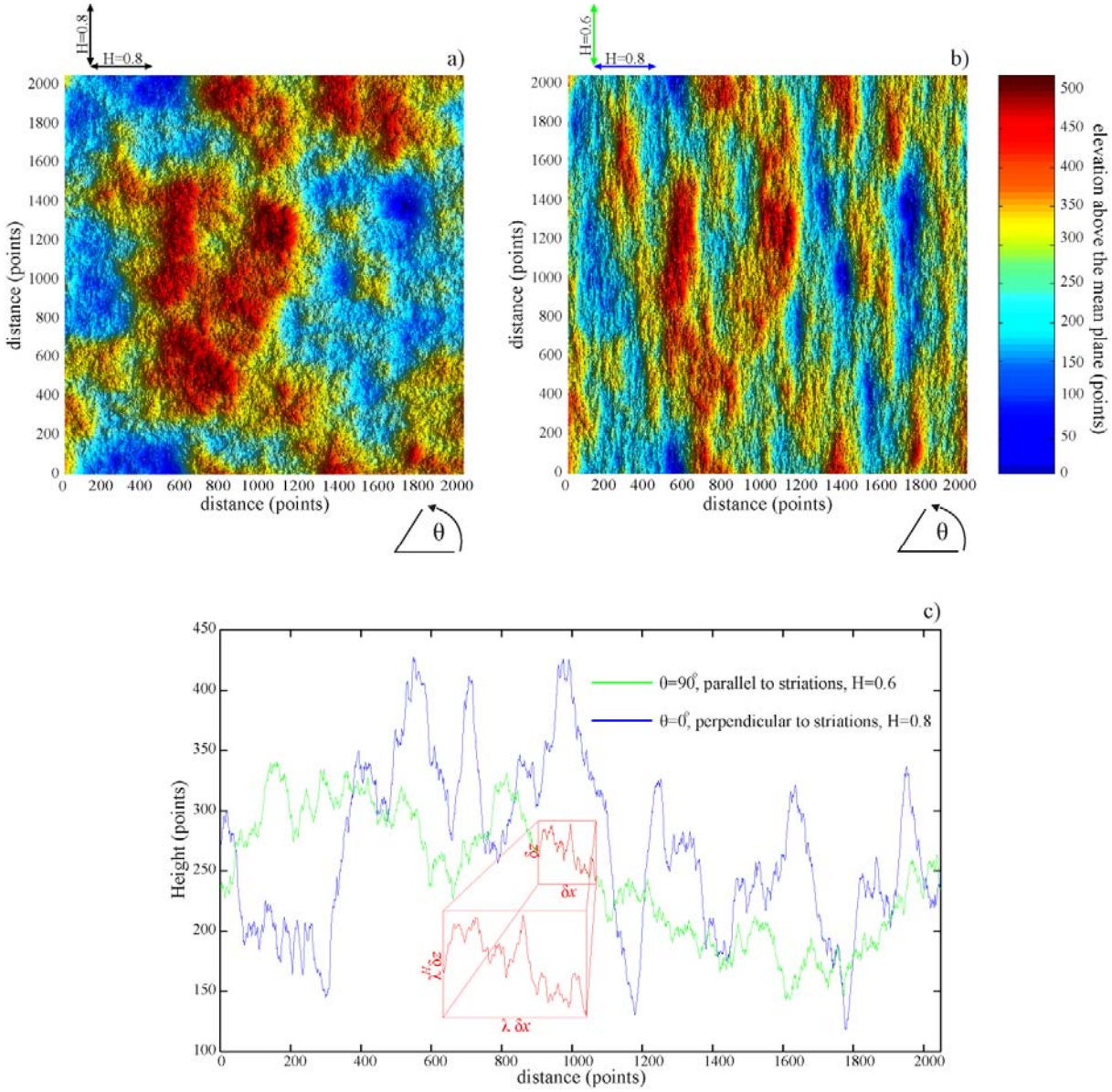

1021

1022 **Figure 1.**

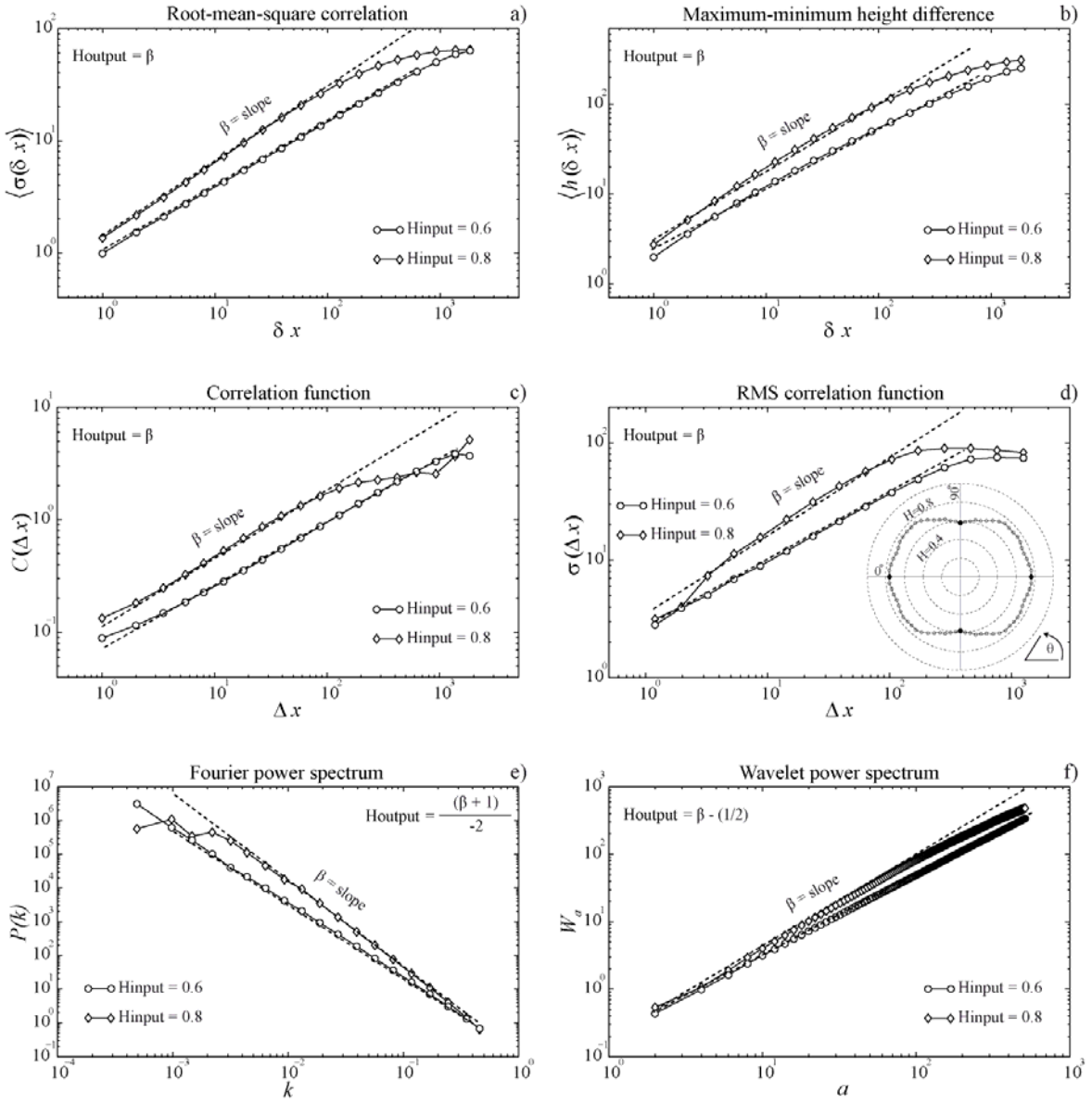

1023

1024 **Figure 2.**

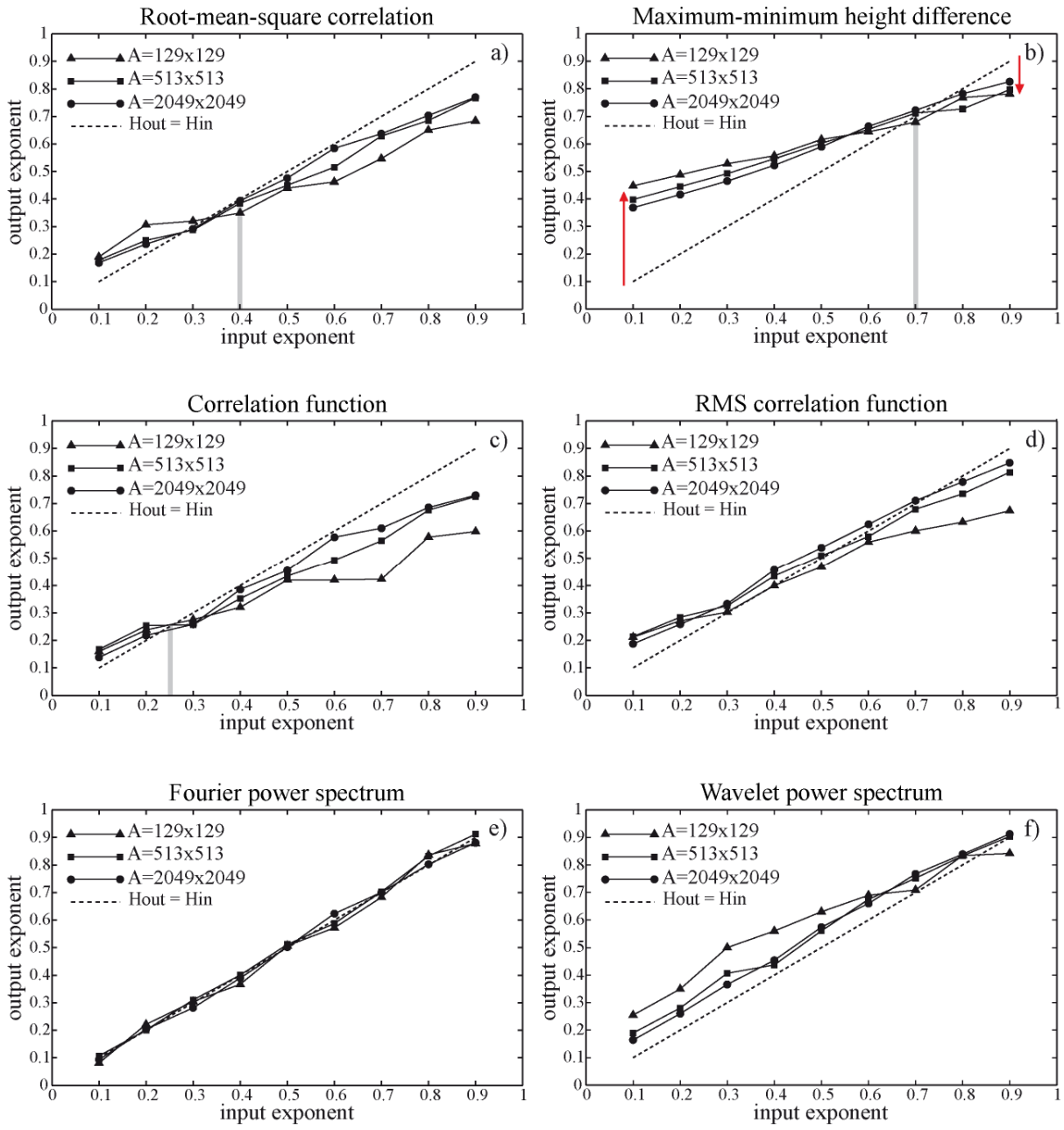

1025

1026 **Figure 3.**

1027

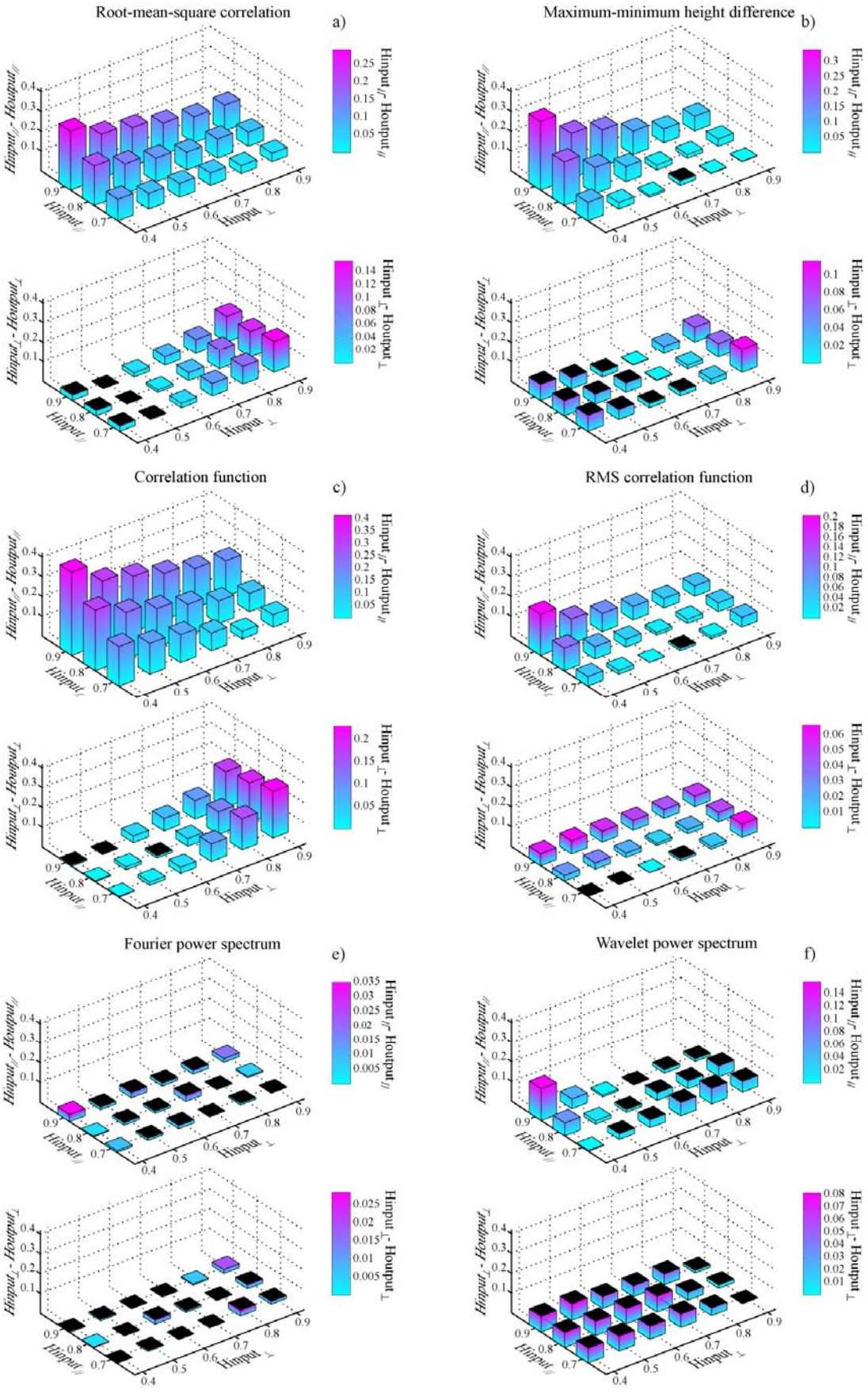
Root-mean-square correlation
a)
Maximum-minimum height difference
b)
Correlation function
c)
RMS correlation function
d)
Fourier power spectrum
e)
Wavelet power spectrum
f)
Hinput// - Houtput//
Hinput⊥ - Houtput⊥
Hinput// - Houtput⊥
Hinput⊥ - Houtput//
Hinput// Houtput//
Hinput⊥ Houtput⊥
Hinput// Houtput⊥
Hinput⊥ Houtput//
Hinput//
Hinput⊥

Figure 4.

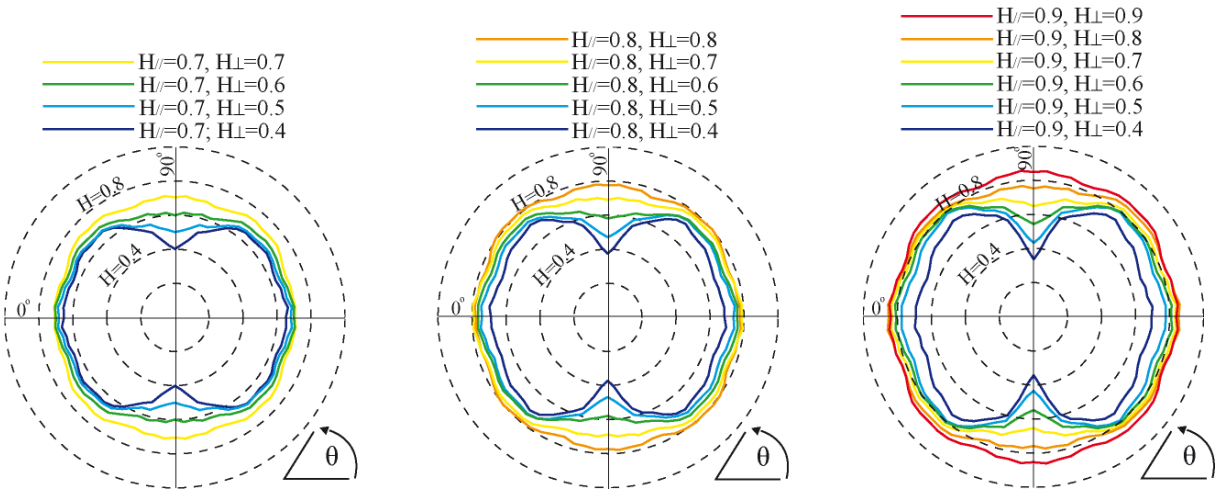

1031

1032 **Figure 5.**

1033

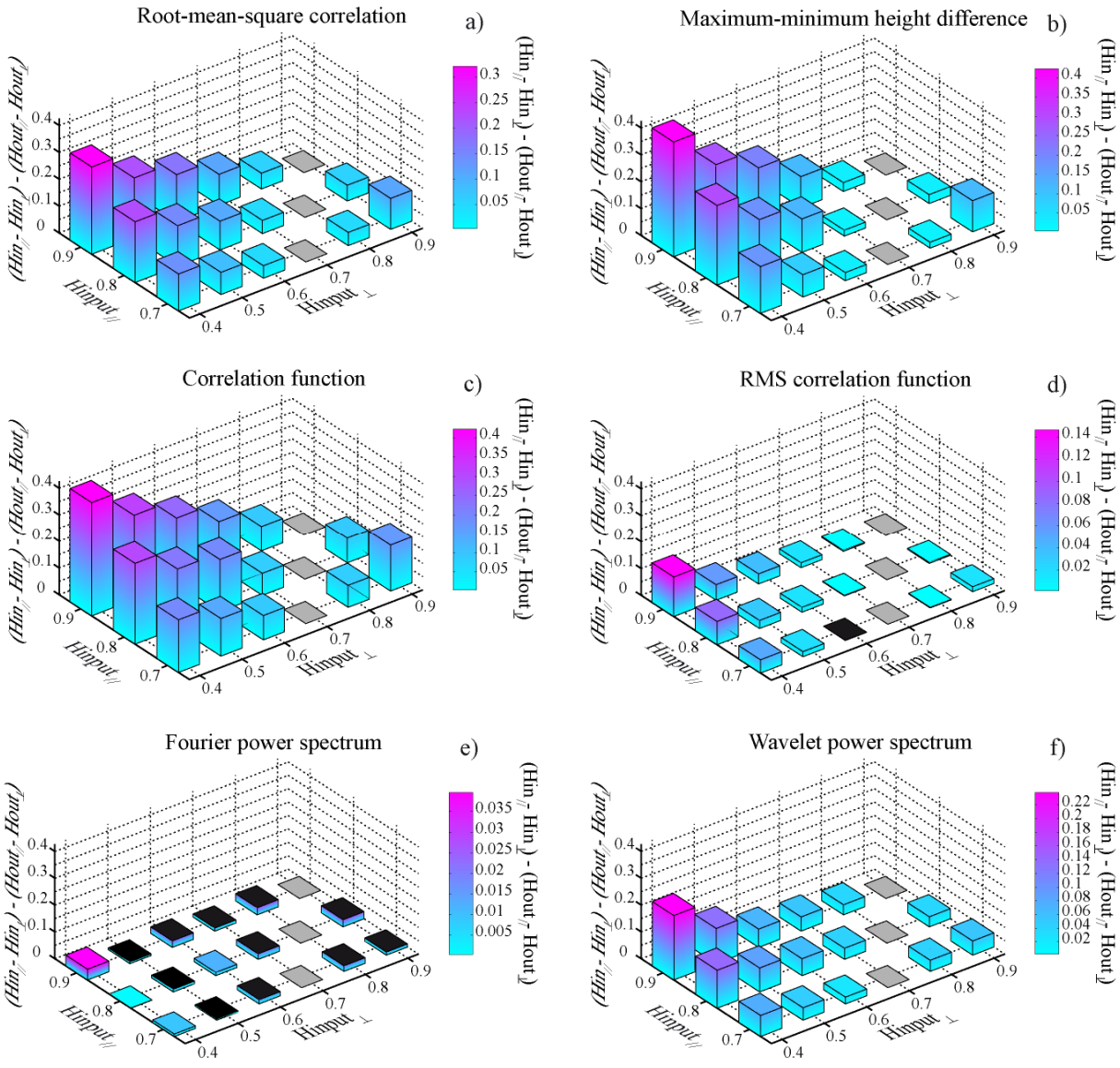
Root-mean-square correlation
a)
Maximum-minimum height difference
b)
Correlation function
c)
RMS correlation function
d)
Fourier power spectrum
e)
Wavelet power spectrum
f)
(Hin// - Hin//) - (Hout// - Hout//)
(Hin⊥ - Hin⊥) - (Hout⊥ - Hout⊥)
Hinput//
Hinput⊥

Figure 6.

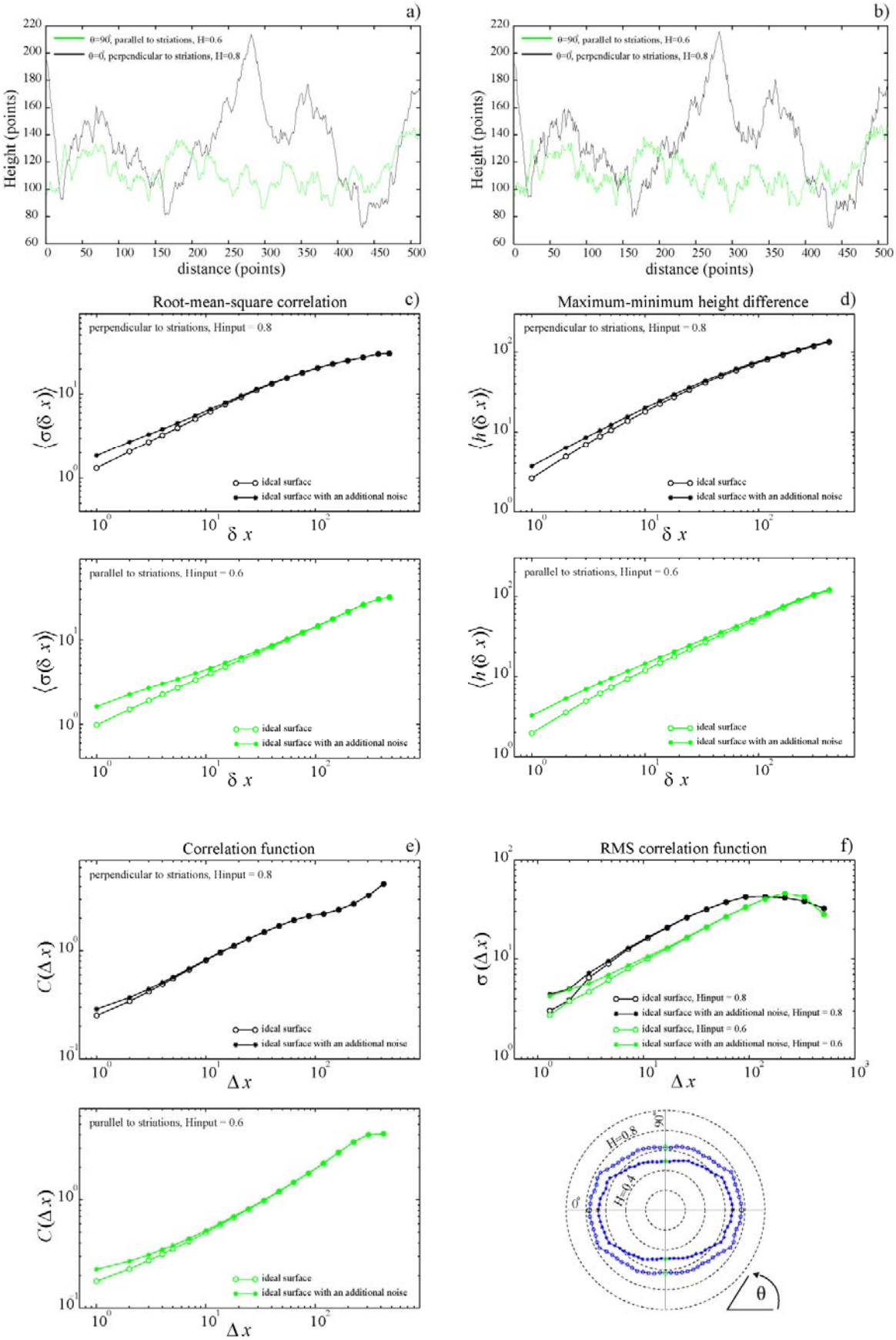
a)
b)
θ=90̊, parallel to striations, H=0.6
θ=0̊, perpendicular to striations, H=0.8
Height (points)
distance (points)
Root-mean-square correlation
c)
Maximum-minimum height difference
d)
perpendicular to striations, Hinput = 0.8
parallel to striations, Hinput = 0.6
ideal surface
ideal surface with an additional noise
⟨σ(δ x)⟩
⟨h(δ x)⟩
δ x
Correlation function
e)
RMS correlation function
f)
C(Δ x)
σ(Δ x)
Δ x
ideal surface, Hinput = 0.8
ideal surface with an additional noise, Hinput = 0.8
ideal surface, Hinput = 0.6
ideal surface with an additional noise, Hinput = 0.6
H=0.8
H=0.4
θ

1036

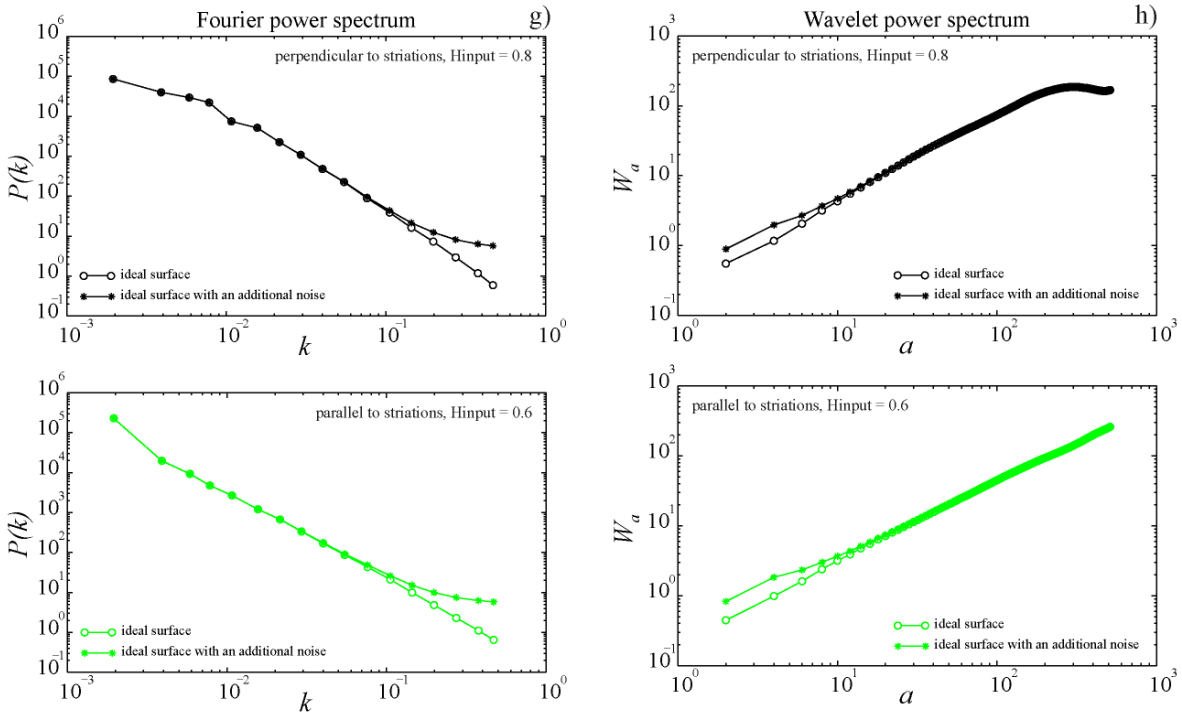

1037

1038 **Figure 7.**

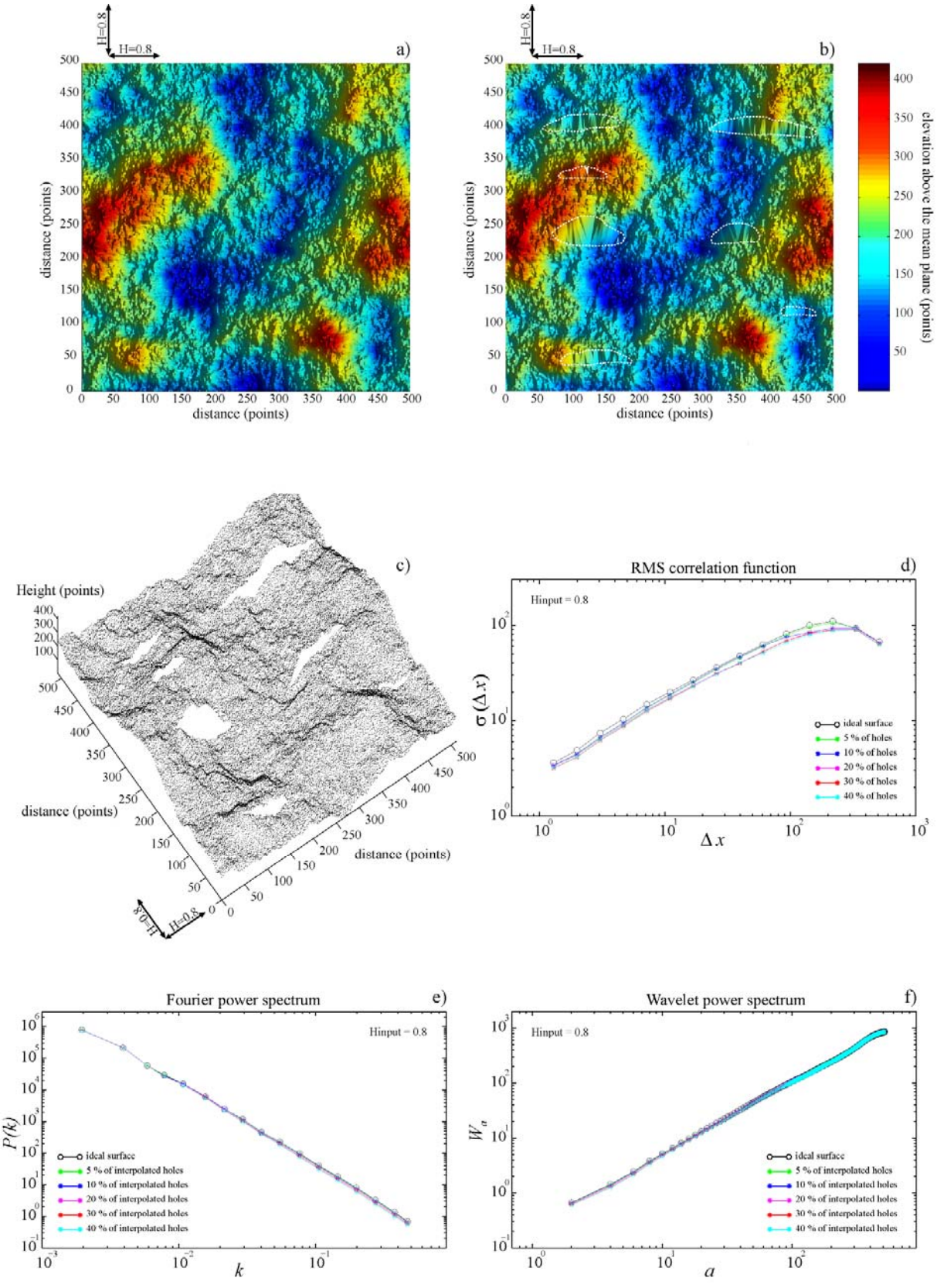
a)
b)
c)
d)
e)
f)
H=0.8
distance (points)
elevation above the mean plane (points)
Height (points)
RMS correlation function
Hinput = 0.8
σ(Δx)
Δx
ideal surface
5 % of holes
10 % of holes
20 % of holes
30 % of holes
40 % of holes
Fourier power spectrum
P(k)
k
5 % of interpolated holes
10 % of interpolated holes
20 % of interpolated holes
30 % of interpolated holes
40 % of interpolated holes
Wavelet power spectrum
W_a
a

Figure 8.

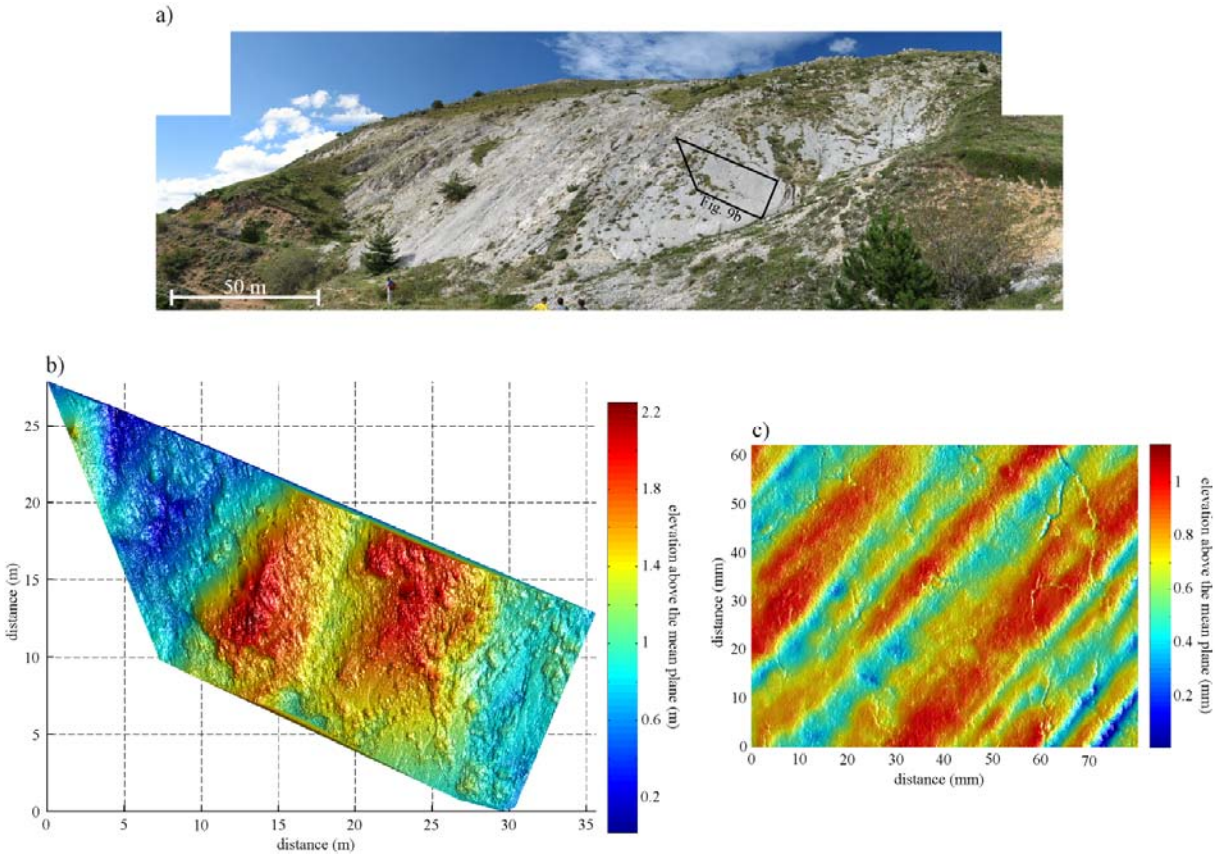

1041

1042 **Figure 9.**

1043

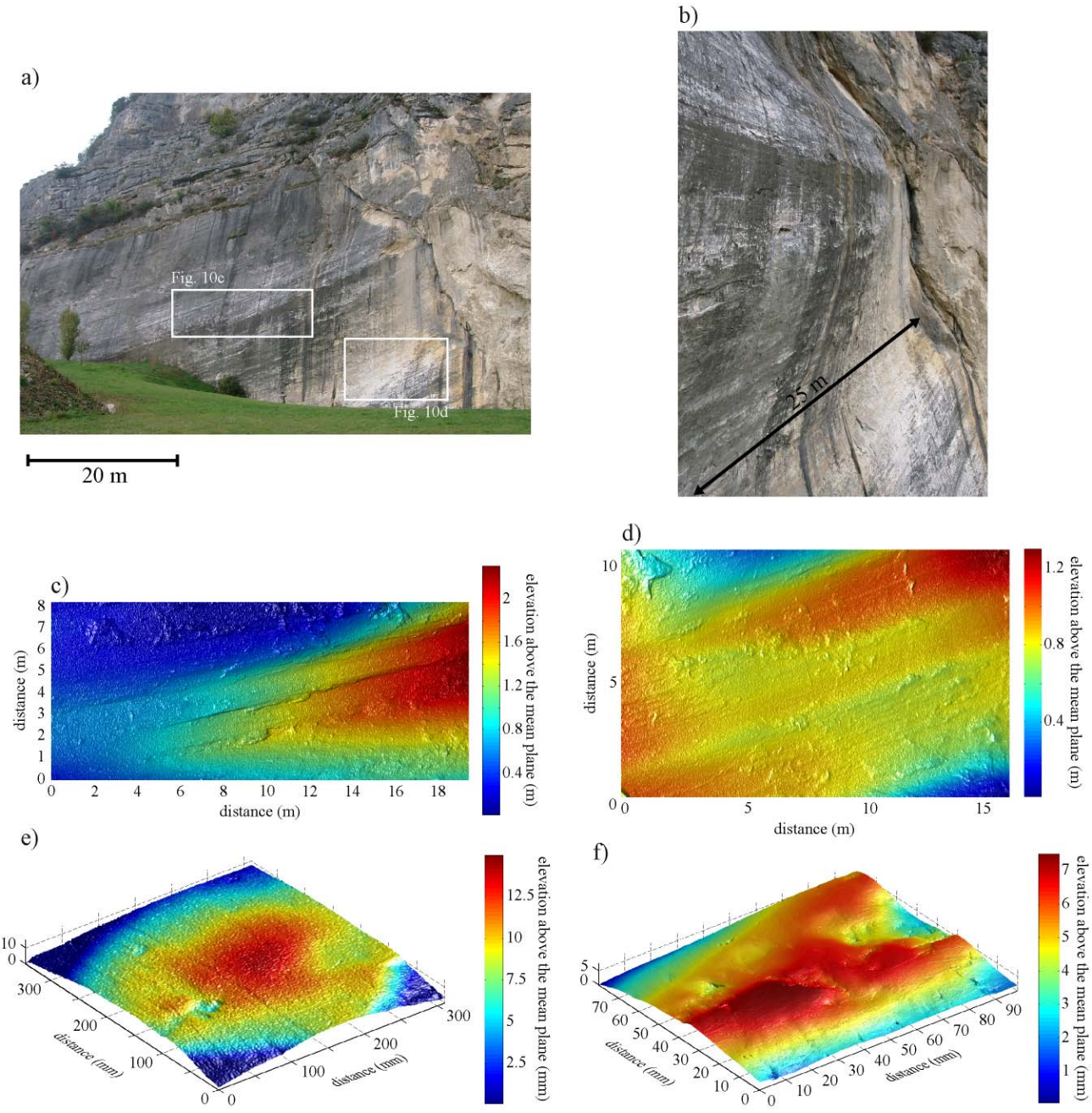
a)
Fig. 10c
Fig. 10d
20 m
b)
25 m
c)
distance (m)
distance (m)
elevation above the mean plane (m)
d)
distance (m)
distance (m)
elevation above the mean plane (m)
e)
distance (mm)
distance (mm)
elevation above the mean plane (mm)
f)
distance (mm)
distance (mm)
elevation above the mean plane (mm)

Figure 10.

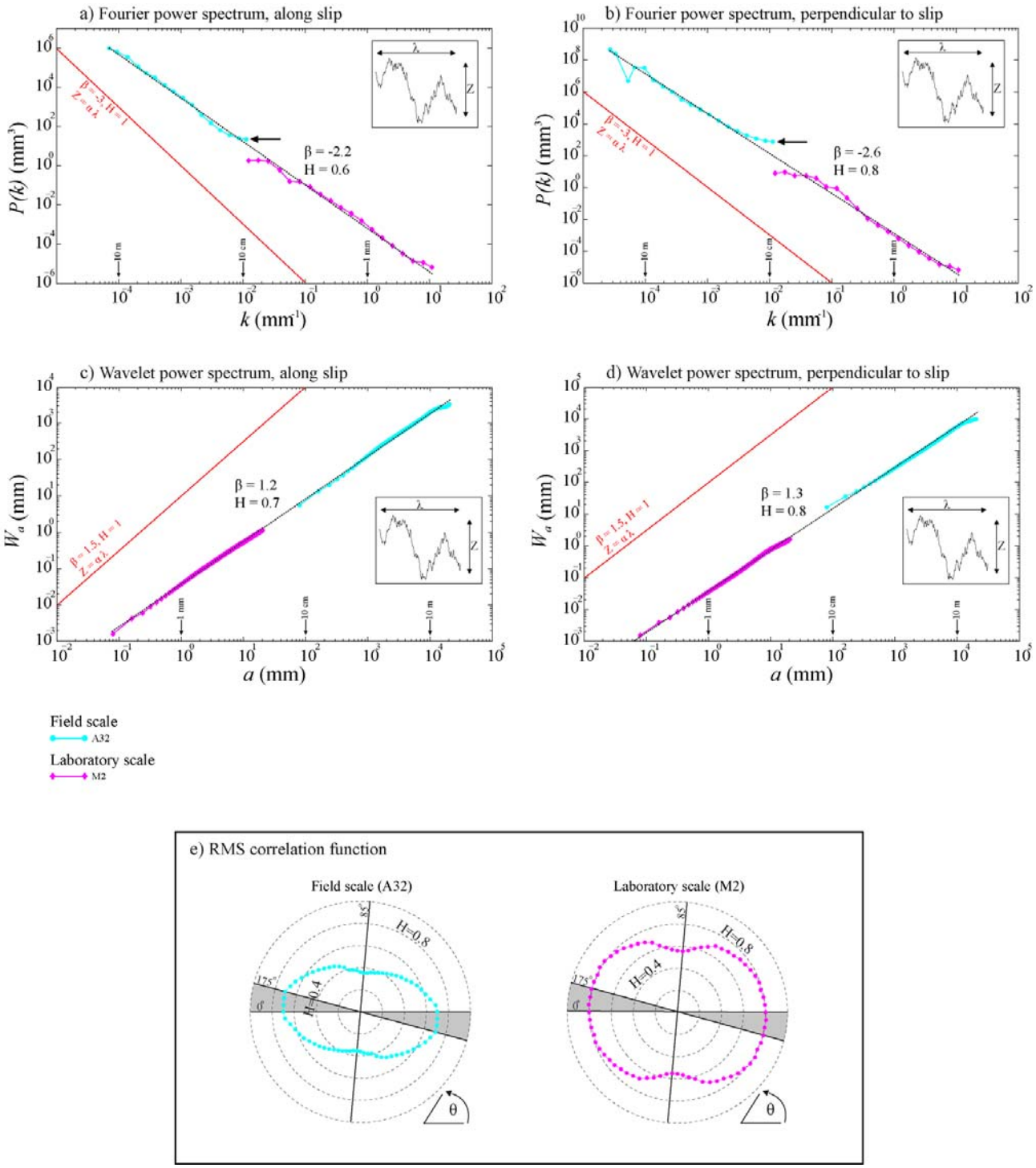

1047

1048 **Figure 11.**

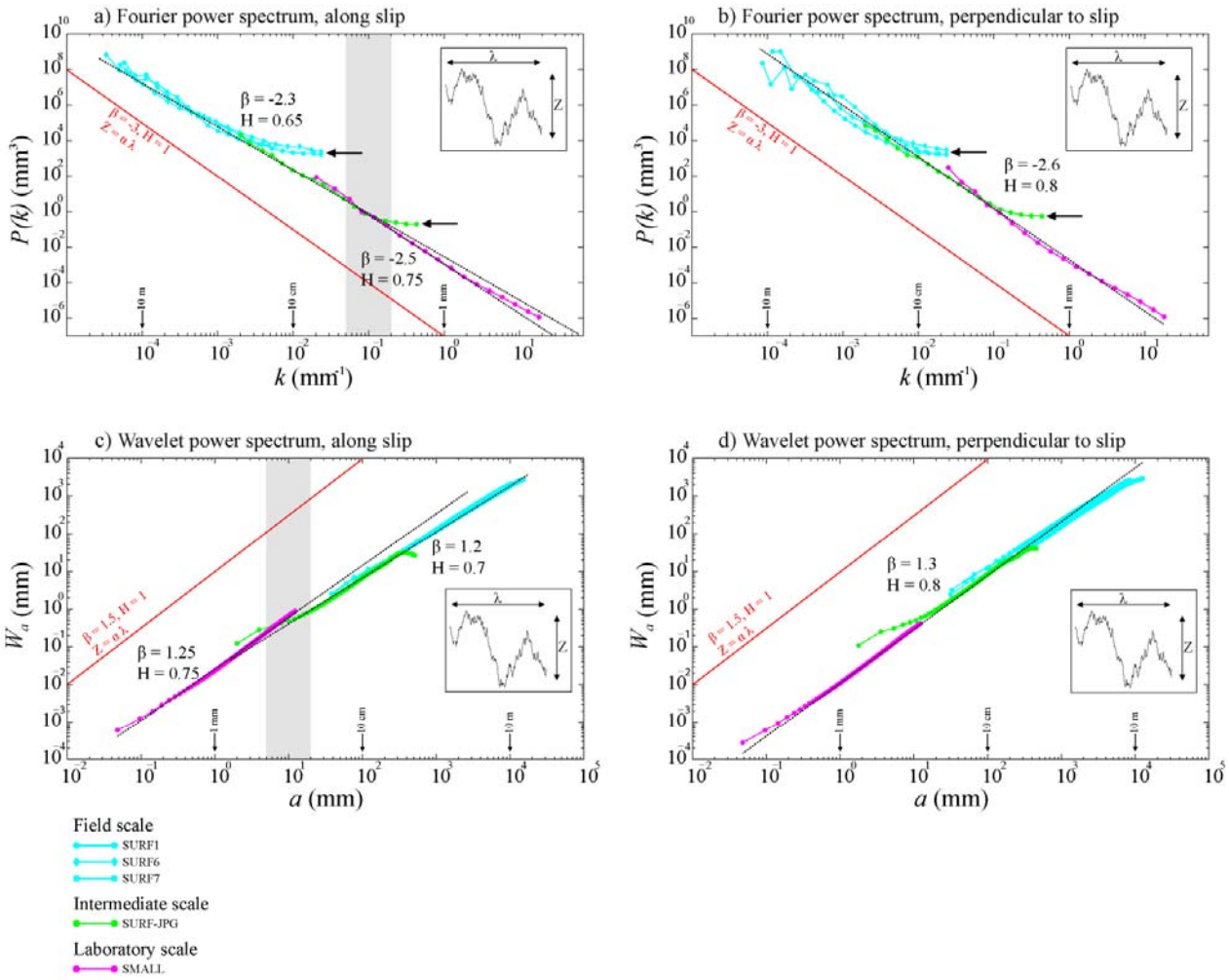

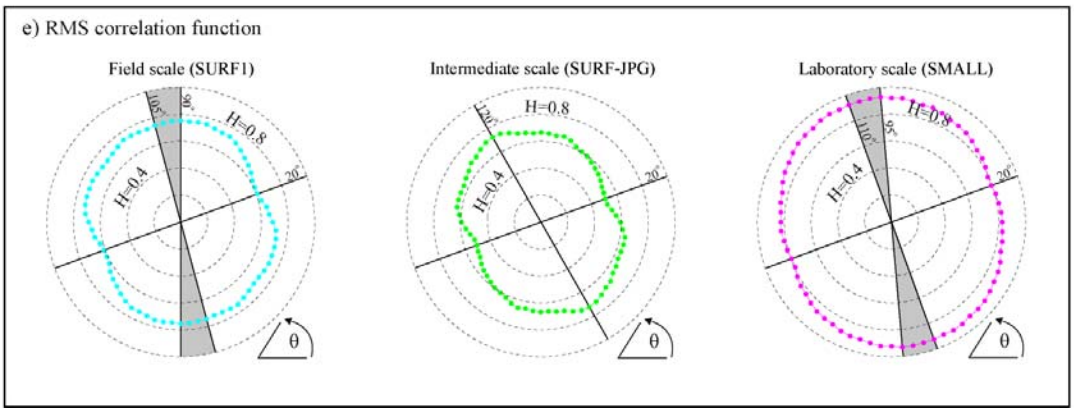

1049

1050 **Figure 12.**